Computer Methods in Applied Mechanics and Engineering 463 (2027) 119339

Contents lists available at ScienceDirect

Comput. Methods Appl. Mech. Engrg.

journal homepage: www.elsevier.com/locate/cma

Stabilized isogeometric mixed material point method for modeling coupled diffusion and deformation in hydrogels

Ashkan Ali Madadi [a,*], Thomas J.R. Hughes [a,b], Rui Huang [b]

[a] Oden Institute for Computational Engineering and Sciences, The University of Texas at Austin, Austin, TX, USA
[b] Department of Aerospace Engineering and Engineering Mechanics, The University of Texas at Austin, Austin, TX, USA

ARTICLE INFO

Keywords:
Material point method
Isogeometric analysis
Hydrogel
Diffusion
Instability and bifurcation

ABSTRACT

In response to external stimuli, hydrogels undergo large deformation coupled with solvent diffusion. The chemomechanical coupling produces transient, strongly nonlinear responses that can trigger instabilities and bifurcations. Modeling such responses using conventional Finite Element Methods (FEMs) often breaks down due to significant mesh distortion. Here, we present an implicit, mixed material point method (MPM) grounded in non-equilibrium thermodynamics that remains robust under large distortions while consistently coupling deformation and solvent diffusion. Cut-cell ill-conditioning near boundaries is removed using extended B-splines that interpolate *boundary* degrees of freedom from *interior* ones via Lagrange polynomials, and subdivision-stabilized interpolation of displacement and chemical potential provides an *inf–sup* stable discretization. Essential boundary conditions are imposed weakly through a symmetric Nitsche formulation on boundary material points. Together, these improvements yield a symmetric, well-conditioned tangent stiffness suitable for eigenvalue-based stability and bifurcation analysis. We demonstrate the stability and accuracy of the method on benchmark problems, including one-dimensional constrained swelling, swell-induced buckling of a hydrogel column, and bifurcation and surface creasing of a hydrogel with cylindrical pores. The present MPM methodology provides a robust computational foundation for studying extreme, diffusion-coupled deformations in soft-matter applications.

1. Introduction

Hydrogel material systems – ranging from reverse osmosis membranes [1–3] to bio-interfaces [4–6] and soft actuators [7–9] – operate through tightly coupled solvent transport and large deformation. Predicting their behavior requires simulations that remain stable as the gel swells significantly and the topology evolves nonlinearly, often accompanied by instabilities and bifurcations [10–12]. Simulating these deformations requires a robust multiphysics framework that accounts for the chemomechanical coupling and the transient irreversible processes. Mesh–based finite elements and isogeometric methods have delivered many successes [13–15], but the kinematics of extremely large deformation poses two recurring challenges: severe mesh distortion [16] and self-contact [17]. Hybrid Eulerian–Lagrangian particle frameworks, and the Material Point Method (MPM) in particular, avoid mesh distortion by solving the problem on a fixed Eulerian background grid while storing history variables and performing numerical integration on Lagrangian material points [18]. MPM naturally accommodates large deformations and no–slip contact without specialized mortar or search algorithms, making it attractive for simulating extremely large deformations. However, MPM has difficulty capturing structural instabilities — such as buckling, wrinkling, and creasing — arising from the highly nonlinear material responses and

* Corresponding author.
E-mail address: ashkan31194@utexas.edu (A. Ali Madadi).

https://doi.org/10.1016/j.cma.2026.119339
Received 17 June 2026; Received in revised form 31 July 2026; Accepted 19 August 2026
Available online 2 September 2026

geometric effects. These instabilities lead to bifurcations or a loss of strong ellipticity in the sense of Hill [19] and Biot [20]. The challenge is further exacerbated by the coupled nature of the field equations governing displacement $\mathbf{u}$ and chemical potential μ, leading to indefinite systems that are prone to numerical instability under certain loading conditions. Several studies have been conducted in the context of FEM to assess the stability of solutions in mixed $\mathbf{u}-p$ formulations for nearly incompressible materials, where p denotes the pressure-like Lagrange multiplier field enforcing near-incompressibility [21–23], and in mixed $\mathbf{u}-\mu$ formulations for hydrogels, where μ denotes the solvent chemical potential [15]. In MPM, such developments are only beginning to appear — for example, the recent $\mathbf{u}-p$ formulation by Ali Madadi and Dortdivanlioglu [24] — but an analogous $\mathbf{u}-\mu$ treatment for hydrogels has not been reported to our knowledge. Due to numerical instabilities, classical eigenvalue analysis is often infeasible in MPM, hindering the detection of the critical points for bifurcation. To overcome this challenge, the development of stabilization techniques is required to improve the conditioning of the stiffness matrix in MPM.

A key issue of MPM, recognized early on, is the cell-crossing error [25] associated with C^0 Lagrange shape functions: when a material point moves from one cell to an adjacent cell, the discontinuity of shape-function gradients can induce spurious energy oscillations. Among the variants proposed to mitigate this issue — GIMP [26], CPDI [27–29], DDMP [30–33], and B-spline MPM (analogous to isogeometric analysis) [25,34–43] — the B-spline MPM appears especially viable due to its higher-order, high-regularity bases and rigorous $h/p/k/r$-refinement machinery [44,45]. However, numerical challenges remain for isogeometric MPM, particularly with implicit solvers, which are often preferred for their unconditional stability in time-stepping.

First, imposing essential boundary conditions is challenging in MPM due to its immersed (embedded) domain nature [46]. In conforming mesh-based methods, Dirichlet boundary conditions are enforced strongly at nodal degrees of freedom; in immersed methods, where the physical boundary does not align with the background grid, these conditions must be imposed *weakly*, typically on surface material points. Three common weak-enforcement techniques are the Lagrange multiplier method [47–51], the penalty method [52,53], and Nitsche's method [24,39,54–58]. The Lagrange-multiplier method is rigorous and versatile but introduces additional unknowns, leading to a mixed formulation that must satisfy the *inf–sup* condition and may require special interpolation or stabilization. The penalty method is simple and does not introduce extra fields, but it is inconsistent with the strong form and often requires a large penalty to reduce errors, which can worsen conditioning. Nitsche's method provides a consistent alternative by augmenting the weak form with flux (consistency) terms and, in symmetric variants, additional symmetric terms; it preserves consistency, allows smaller penalty parameters, and generally improves accuracy and convergence [59].

Second, cut cells at boundaries yield ill-conditioned stiffness matrices, degrading stability and Newton–Raphson convergence. This effect is amplified when using Nitsche's method, necessitating very large penalty parameters. Two rigorous remedies to resolve the *cut-cell instability* are ghost stabilization [60–62] and extended B-splines [39,63–67]. The ghost stabilization technique introduces penalty terms that suppress discontinuities in the solution across faces of cut cells, thereby restoring smoothness and controlling the conditioning of the stiffness matrix. While effective, it increases formulation complexity by augmenting the weak form with additional stabilization terms. Extended B-splines provide an alternative by redefining the basis: boundary degrees of freedom are extrapolated from a local block of interior control points via Lagrange interpolation, consistent with Marsden's theorem [68,69], restoring completeness and conditioning without additional stabilization terms.

The other numerical challenge that we should consider in mixed variational formulations, such as displacement and chemical potential, is to ensure *inf–sup* stability due to an indefinite system of equations [70,71]. Arbitrary combinations of interpolation spaces for different fields can lead to numerical instabilities, including spurious chemical potential oscillations and inaccurate coupling between variables. Classical FEM approaches such as Taylor–Hood elements have been shown to be unstable in IGA settings when the full continuity of B-spline basis functions is preserved [72–76]. While C^{-1}-discontinuous Taylor–Hood-type discretizations for pressure (or chemical potential) can satisfy the *inf–sup* condition in IGA [77], the reduced continuity introduces cell-crossing errors in the context of immersed methods. To resolve this issue while retaining the superior continuity properties of IGA, Rüberg and Cirak [65,78] proposed *subdivision B-spline* shape functions. This method leverages the two-scale relation between coarse and fine B-spline spaces to construct *inf–sup* stable mixed discretizations without modifying the underlying knot vector or introducing additional fields. This approach, mathematically proved to be *inf–sup* stable [75,76], maintains the high-order accuracy and highest possible smoothness of IGA while ensuring numerical robustness for multiphysics coupling in large deformation problems.

In this work, we develop a stabilized MPM framework for coupled large deformation and solvent transport in hydrogels, building on a robust non-equilibrium multiphysics theory [79–81]. To address the numerical challenges in MPM, we use mixed, subdivision-stabilized *extended* B-spline shape functions together with Nitsche's imposition of essential boundary conditions. The subdivision construction yields an *inf–sup* stable discretization, which is critical when the gel behaves as a nearly incompressible solid in the short time limit. Using the extended B-splines for both displacement and chemical-potential fields improves the conditioning of the global stiffness matrix. We adopt the *symmetric* Nitsche variant: although generally less robust than the skew-symmetric form, it produces a symmetric coupled tangent, which, combined with the extended and subdivision bases, yields a well-conditioned operator suitable for efficient eigenvalue analysis. For stability assessment, we follow Dortdivanlioglu and Linder [15] and track the signature (inertia) of the *full* stiffness matrix, which is simpler and cheaper than computing the smallest eigenvalue of the reduced (Schur-complement) stiffness matrix, thereby facilitating stability analysis in mixed formulations. To our knowledge, this is the first application of MPM to hydrogels with an implicit mixed $\mathbf{u}-\mu$ formulation; together with the above stabilizations, it enables simulations of complex phenomena such as bifurcation and creasing.

The remainder of the paper is organized as follows: Section 2 presents the formulation of governing equations, variational structure, and constitutive model. The computational framework is detailed in Section 3: Section 3.1 describes the weak imposition of boundary conditions; Section 3.2 and Section 3.3 present MPM discretization and linearization; Section 3.4 and Section 3.5 introduce the subdivision and extended B-spline constructions; Section 3.6 outlines the stability check. A series of numerical examples in Section 4 demonstrate the robustness of the present MPM method, followed by conclusions in Section 5.

2. Theoretical formulation

This section presents the governing equations for a multiphysics mixed formulation tailored to hydrogels, where each continuum material point is associated with a deformation mapping $\boldsymbol{\varphi}$ from the reference to the current configuration, a local solvent concentration C, and its conjugate chemical potential μ. A two-field mixed $\mathbf{u}$–μ formulation is employed to model the coupled deformation and solvent transport within a polymer network [79,80]. The free energy density of the gel is described using the Flory–Rehner model, while solvent transport is governed by Fick's law, driven by gradients in the chemical potential.

2.1. Governing equations

In the reference (material) configuration, the hydrogel occupies a domain Ω_d, and each material particle is labeled by its location $\mathbf{X}\in\Omega_d$. Here, we choose the dry polymer network as the reference configuration for the gel. In the current (spatial) configuration at time t, the gel is subject to mechanical loads and chemical stimuli. Let $\Omega(t)$ be the spatial domain of the current configuration. The mapping $\boldsymbol{\varphi}$ sends a material point $\mathbf{X}\in\Omega_d$ to its current spatial position $\mathbf{x} = \boldsymbol{\varphi}(\mathbf{X},t)\in\Omega(t)$. The displacement is $\mathbf{u}(\mathbf{X},t) = \mathbf{x}-\mathbf{X}$ and the deformation gradient

$$\mathbf{F} = \frac{\partial \mathbf{x}}{\partial \mathbf{X}} = \mathbf{I} + \boldsymbol{\nabla}\mathbf{u}. \tag{1}$$

In the current configuration, each material point contains solvent molecules, described by a nominal solvent concentration $C(\mathbf{X},t)$ (number of solvent molecules per unit reference volume). Correspondingly, the chemical potential of the solvent is $\mu(\mathbf{X},t)$.

The free energy density of the hydrogel, denoted by W, is taken to be a function of the deformation gradient $\mathbf{F}$ and the solvent concentration C. The time derivative of W is given by

$$\dot{W} = \mathbf{P} : \dot{\mathbf{F}} + \mu\dot{C}, \tag{2}$$

where $\mathbf{P} = \partial W/\partial \mathbf{F}$ is the nominal stress and $\mu = \partial W/\partial C$ is the chemical potential.

The conservation of solvent molecules requires that

$$\dot{C} + \boldsymbol{\nabla}\cdot\mathbf{J} = 0, \tag{3}$$

where $\mathbf{J}$ is the nominal flux of solvent.

For irreversible processes, the thermodynamic inequality requires that

$$\int_{\Omega_d} \dot{W}\,\mathrm{d}V - \int_{\Omega_d} \mathbf{B}\cdot\dot{\mathbf{u}}\,\mathrm{d}V - \int_{\partial\Omega_d} \mathbf{T}\cdot\dot{\mathbf{u}}\,\mathrm{d}A - \int_{\partial\Omega_d} \mu\, i\,\mathrm{d}A \le 0, \tag{4}$$

where $\mathbf{B}$ denotes the body force per unit reference volume, $\mathbf{T}$ is the nominal traction vector acting on the boundary $\partial\Omega_d$, and i represents the inward flux of solvent across the boundary. We have assumed no internal sources and neglected inertia.

Combining the above equations and applying the divergence theorem, we obtain

$$\int_{\Omega_d} -\underbrace{(\boldsymbol{\nabla}\cdot\mathbf{P}+\mathbf{B})}_{=0}\cdot\dot{\mathbf{u}}\,\mathrm{d}V + \int_{\partial\Omega_d}\underbrace{(\mathbf{P}\mathbf{N}-\mathbf{T})}_{=0}\cdot\dot{\mathbf{u}}\,\mathrm{d}A - \int_{\partial\Omega_d}\mu\underbrace{(i+\mathbf{J}\cdot\mathbf{N})}_{=0}\,\mathrm{d}A + \int_{\Omega_d}\underbrace{\mathbf{J}\cdot\boldsymbol{\nabla}\mu}_{<0}\,\mathrm{d}V \le 0 \tag{5}$$

The condition of mechanical equilibrium requires that

$$\boldsymbol{\nabla}\cdot\mathbf{P} + \mathbf{B} = 0 \tag{6}$$

in Ω_d and

$$\mathbf{P}\mathbf{N} = \mathbf{T} \tag{7}$$

on $\partial\Omega_d$. The inward flux of solvent on the boundary $\partial\Omega_d$ is

$$i = -\mathbf{J}\cdot\mathbf{N}, \tag{8}$$

where $\mathbf{N}$ is the unit normal vector pointing outwards.

The mechanical equilibrium is a partial equilibrium for the gel. As long as the chemical potential of the solvent is not constant, the gel is not in chemical equilibrium, and the solvent molecules migrate in the gel. The thermodynamic inequality becomes

$$\int_{\Omega_d} \mathbf{J}\cdot\boldsymbol{\nabla}\mu\mathrm{d}V \le 0. \tag{9}$$

To satisfy this inequality for arbitrary gradients in chemical potential, we adopt a constitutive law for the nominal solvent flux of the form

$$\mathbf{J} = -\mathbf{M}\,\boldsymbol{\nabla}\mu, \tag{10}$$

where $\mathbf{M}$ is a positive definite mobility tensor. In general, $\mathbf{M}$ is a function of $\mathbf{F}$ and C.

For computational convenience, the free energy function can be reformulated in terms of chemical potential rather than solvent concentration by applying a Legendre transform:

$$\widehat{W}(\mathbf{F},\mu) = W(\mathbf{F},C) - \mu C. \tag{11}$$

As a result, the constitutive relations can be re-written in terms of the deformation gradient and chemical potential:

$$\mathbf{P} = \frac{\partial \widehat{W}(\mathbf{F},\mu)}{\partial \mathbf{F}}, \quad C = -\frac{\partial \widehat{W}(\mathbf{F},\mu)}{\partial \mu}. \tag{12}$$

We further assume that the polymer network is incompressible and that any changes in the volume of the gel arise solely from variations in the solvent concentration, i.e., $\det \mathbf{F} = 1 + \upsilon C$, where υ is the molecular volume of solvent. To enforce this constraint, we re-write the free energy function $\widehat{W}$ as:

$$\widehat{W}(\mathbf{F},\mu) = W(\mathbf{F}, \frac{\det \mathbf{F} - 1}{\upsilon}) - \frac{\mu}{\upsilon}(\det \mathbf{F} - 1). \tag{13}$$

To summarize, the strong form of the governing equations are:

$$\begin{aligned} &\mathbf{F} = \mathbf{I} + \boldsymbol{\nabla}\mathbf{u}, \quad \det \mathbf{F} = 1 + \upsilon C, \\ &\boldsymbol{\nabla}\cdot\mathbf{P} + \mathbf{B} = 0, \quad \mathbf{P} = \partial_{\mathbf{F}}\widehat{W}, \\ &\partial_t C + \boldsymbol{\nabla}\cdot\mathbf{J} = 0, \quad \mathbf{J} = -\mathbf{M}\boldsymbol{\nabla}\mu, \end{aligned} \tag{14}$$

in Ω_d, and

$$\begin{aligned} &\mathbf{P}\mathbf{N} = \mathbf{T}, \\ &\mathbf{J}\cdot\mathbf{N} = -i, \end{aligned} \tag{15}$$

on $\partial\Omega_d$.

Correspondingly, we obtain the weak form using the test functions, $\hat{\mathbf{u}}$ and $\hat{\mu}$, for the displacement and chemical potential fields, respectively:

$$\mathcal{G}(\mathbf{u},\mu;\hat{\mathbf{u}}) = \int_{\Omega_d} \mathbf{P}(\mathbf{F},\mu) : \boldsymbol{\nabla}\hat{\mathbf{u}}\,\mathrm{d}V - \int_{\Omega_d} \mathbf{B}\cdot\hat{\mathbf{u}}\,\mathrm{d}V - \int_{\partial\Omega_d} \mathbf{T}\cdot\hat{\mathbf{u}}\,\mathrm{d}A = 0, \tag{16}$$

and

$$\dot{\mathcal{H}}(\mathbf{u},\mu;\hat{\mu}) = \int_{\Omega_d} -\left(\frac{\partial C}{\partial t}\hat{\mu} + \mathbf{M}\boldsymbol{\nabla}\mu\cdot\boldsymbol{\nabla}\hat{\mu}\right)\mathrm{d}V + \int_{\partial\Omega_d} i\,\hat{\mu}\,\mathrm{d}A = 0. \tag{17}$$

2.2. Free energy function

The free energy density function by the Flory–Rehner model is adopted for the hydrogel, which incorporates two key contributions: the elastic energy of the polymer network and the free energy of mixing polymer and solvent molecules. The total free energy per unit reference volume is given by

$$W(\mathbf{F},C) = \underbrace{\frac{1}{2}Nk_BT\,(\mathbf{F}:\mathbf{F} - 2\log(\det\mathbf{F}) - 3)}_{\text{Polymer elasticity (Neo-Hookean)}} \underbrace{- \frac{k_BT}{\upsilon}\left[\upsilon C\log\left(1 + \frac{1}{\upsilon C}\right) + \frac{\chi}{1+\upsilon C}\right]}_{\text{Polymer-solvent mixing (Flory–Huggins)}}, \tag{18}$$

where N is the number density of elastically active polymer chains (network strands) in the reference configuration, k_B is Boltzmann's constant, T is the absolute temperature, and χ is the Flory–Huggins interaction parameter describing polymer–solvent affinity.

By eliminating the solvent concentration C with the incompressibility constraint, $\det\mathbf{F} = 1 + \upsilon C$, and applying the Legendre transform, we obtain the free energy density in terms of the chemical potential μ:

$$\widehat{W}(\mathbf{F},\mu) = \frac{1}{2}Nk_BT\,(\mathbf{F}:\mathbf{F} - 2\log(\det\mathbf{F}) - 3) - \frac{k_BT}{\upsilon}\left[(\det\mathbf{F} - 1)\log\left(\frac{\det\mathbf{F}}{\det\mathbf{F} - 1}\right) + \frac{\chi}{\det\mathbf{F}}\right] - \frac{\mu}{\upsilon}(\det\mathbf{F} - 1). \tag{19}$$

2.3. Mobility tensor

We adopt Fick's law to define the mobility tensor $\mathbf{M}$. In the current configuration, the true flux $\mathbf{j}$ is linearly proportional to the spatial gradient of the chemical potential by Fick's law:

$$\mathbf{j} = -\frac{cD}{k_BT}\boldsymbol{\nabla}_{\mathbf{x}}\mu, \tag{20}$$

where c is the true solvent concentration in the current configuration and D is the diffusion coefficient of the solvent.

With respect to the reference configuration, the nominal flux is related to the material gradient of the chemical potential, Eq. (10), with a mobility tensor given by Fick's law:

$$\mathbf{M} = \frac{CD}{k_BT}(\mathbf{F}^T\mathbf{F})^{-1}. \tag{21}$$

Since $C > 0$ and $\mathbf{F}^T\mathbf{F}$ is positive definite, the mobility tensor $\mathbf{M}$ is positive definite as long as $D > 0$.

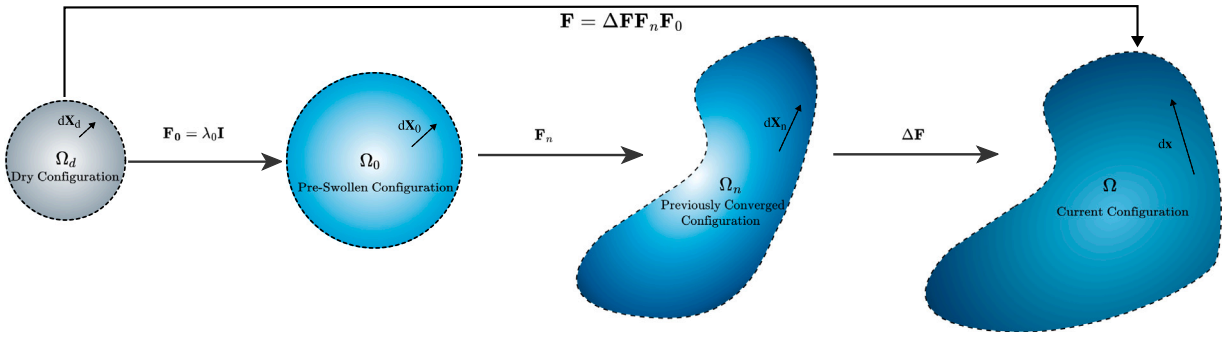

Fig. 1. Kinematic decomposition of the deformation gradient. Here, $\mathbf{F}_0$ maps from the dry reference configuration to the pre-swollen initial configuration at $t = 0$, $\mathbf{F}_n$ maps from the initial to the converged configuration at $t = t_n$, and $\Delta\mathbf{F}$ maps from the converged configuration to the current configuration at $t = t_n + \Delta t$.

2.4. Incremental formulation

The formulations above use the dry state Ω_d (with $C = 0$) as the reference configuration. However, the chemical potential of the solvent is unbounded in the dry state, which cannot be taken as the initial condition for numerical purposes. To avoid this issue, we assume a compatible pre-swollen configuration Ω_0 as the initial state ($t = 0$), which is stress-free and in equilibrium with a finite chemical potential μ_0. This configuration corresponds to an isotropic swelling characterized by $\mathbf{F}_0 = \lambda_0\mathbf{I}$, where $\lambda_0 > 1$ is the initial swelling stretch. Correspondingly, the initial solvent concentration is: $C_0 = (\lambda_0^3 - 1)/\upsilon$, and the initial chemical potential is given by [81]

$$\frac{\mu_0}{k_B T} = N\upsilon\left(\frac{1}{\lambda_0} - \frac{1}{\lambda_0^3}\right) + \log\left(1 - \frac{1}{\lambda_0^3}\right) + \frac{1}{\lambda_0^3} + \frac{\chi}{\lambda_0^6}. \tag{22}$$

Decompose the deformation gradient at time t_n as

$$\mathbf{F}(t_n) = \mathbf{F}_n\,\mathbf{F}_0, \tag{23}$$

where $\mathbf{F}_n$ describes the deformation from the initial configuration Ω_0 to the current configuration Ω_n for $n > 0$.

Following Ali Madadi and Dortdivanlioglu [24,72], we adopt the converged configuration Ω_n as an intermediate reference configuration. In this so-called *previously converged Lagrangian* framework, the configuration Ω_n, which satisfies the governing equations and boundary conditions at the time t_n, is used as the reference for the incremental deformation from time t_n to $t_{n+1} = t_n + \Delta t$. To this end, we write

$$\mathbf{F}_{n+1} = \Delta\mathbf{F}\,\mathbf{F}_n, \qquad \Delta J := \det(\Delta\mathbf{F}), \quad J_n := \det(\mathbf{F}_n), \quad J_{n+1} = \Delta J\, J_n, \tag{24}$$

where $\Delta\mathbf{F} = \mathbf{I} + \boldsymbol{\nabla}_n(\Delta\mathbf{u})$ maps the configuration Ω_n to the configuration Ω_{n+1} at time t_{n+1} and $\Delta\mathbf{u}$ is the incremental displacement. This incremental kinematic description, with the background grid shape functions updated only at the beginning of each time step, is particularly convenient for the MPM formulation.

A schematic illustration of this kinematic construction is shown in Fig. 1. A material line element $\mathrm{d}\mathbf{X}_d \equiv \mathrm{d}\mathbf{X}$ in the dry reference configuration is first mapped to $\mathrm{d}\mathbf{X}_0$ in the pre-swollen initial configuration, then to $\mathrm{d}\mathbf{X}_n$ in the converged configuration at time t_n, and finally to $\mathrm{d}\mathbf{x}$ in the current configuration at time t_{n+1}.

Using this decomposition, the free-energy density originally defined as per unit volume of the dry configuration ($\widehat{W}$) can be rescaled to the free energy per unit volume of the intermediate reference configuration at time t_n ($\widehat{W}_n$) as

$$\widehat{W}_n(\Delta\mathbf{F}, \mu; \mathbf{F}_n, \mathbf{F}_0) = \frac{1}{J_n J_0}\,\widehat{W}(\Delta\mathbf{F}\mathbf{F}_n\mathbf{F}_0, \mu), \tag{25}$$

where $J_0 = \lambda_0^3$. With this rescaling, the weak form of the governing equations in Eqs. (16) and (17) can be re-written with respect to the intermediate reference configuration Ω_n as

$$\mathcal{G}(\mathbf{u}, \mu; \hat{\mathbf{u}}) = \int_{\Omega_n} \mathbf{P}_n : \boldsymbol{\nabla}_n\hat{\mathbf{u}}\,\mathrm{d}V_n - \int_{\Omega_n} \mathbf{B}_n \cdot \hat{\mathbf{u}}\,\mathrm{d}V_n - \int_{\partial\Omega_n} \mathbf{T}_n \cdot \hat{\mathbf{u}}\,\mathrm{d}A_n = 0, \tag{26}$$

$$\mathcal{H}(\mathbf{u}, \mu; \hat{\mu}) = \int_{\Omega_n} -\left(\frac{\partial C_n}{\partial t}\hat{\mu} - \mathbf{j}_n \cdot \boldsymbol{\nabla}_n\hat{\mu}\right)\mathrm{d}V_n + \int_{\partial\Omega_n} i_n\,\hat{\mu}\,\mathrm{d}A_n = 0, \tag{27}$$

where $\mathbf{P}_n$ is the first Piola stress with respect to the intermediate reference configuration Ω_n, $\mathbf{T}_n$ is the corresponding traction on the boundary $\partial\Omega_n$, and $\mathbf{B}_n$ is the body force per unit volume of Ω_n:

$$\mathbf{P}_n = \frac{\partial\widehat{W}_n(\Delta\mathbf{F}, \mu; \mathbf{F}_n, \mathbf{F}_0)}{\partial\Delta\mathbf{F}}, \quad \mathbf{P}_n\mathbf{N}_n = \mathbf{T}_n, \quad \mathbf{B}_n = \frac{\mathbf{B}}{J_n J_0}, \tag{28}$$

with $\mathbf{N}_n$ denoting the unit normal on $\partial\Omega_n$. Similarly, the solvent concentration and the flux are rescaled as

$$C_n = \frac{C}{J_n J_0}, \quad \mathbf{j}_n = -\mathbf{M}_n \boldsymbol{\nabla}_n \mu, \quad i_n = -\mathbf{j}_n \cdot \mathbf{N}_n, \tag{29}$$

where $\mathbf{M}_n = \frac{C_n D}{k_B T}(\Delta\mathbf{F}^T \Delta\mathbf{F})^{-1}$. By the chain rule, we have

$$\boldsymbol{\nabla}_n(\cdot) = (\mathbf{F}_n \mathbf{F}_0)^{-T} \boldsymbol{\nabla}(\cdot), \qquad \mathbf{P}_n = \frac{1}{J_n J_0} \mathbf{P}(\mathbf{F}_n \mathbf{F}_0)^T. \tag{30}$$

Integrate Eq. (27) over time by the implicit backward scheme, and we obtain:

$$\mathcal{H}(\mathbf{u}, \mu; \hat{\mu}) = \int_{\Omega_n} \left(-\frac{\Delta J - 1}{\upsilon} \hat{\mu} + \Delta t \, \mathbf{j}_n \cdot \boldsymbol{\nabla}_n \hat{\mu} \right) \mathrm{d}V_n + \int_{\partial\Omega_n} \Delta t \, i_n \, \hat{\mu} \, \mathrm{d}A_n = 0. \tag{31}$$

The two equations, Eqs. (26) and (31), are to be solved simultaneously for $\mathbf{u}$ and μ at each time step, with known quantities at the previous time step t_n and the prescribed boundary conditions at t_{n+1}.

The formulation presented above is not symmetric by default, as the mobility tensor $\mathbf{M}_n$ depends on the unknown incremental deformation gradient $\Delta\mathbf{F}$. To restore symmetry and ensure consistency with a saddle-point structure, we adopt the common approximation $\mathbf{M}_n \approx m_n \mathbf{I}$, where $m_n = C_n D/(k_B T)$ is evaluated from the previously converged configuration. Thus, the mobility remains deformation-dependent through the evolving state $\mathbf{F}_n$, but its dependence on the unknown incremental deformation within the current time step is neglected. To clarify the effect of this approximation, we decompose the volume integral in the chemical residual $\mathcal{H}$ into $\mathcal{H}^{\mathrm{vol}} + \mathcal{H}^{\mathrm{mob}}$, where $\mathcal{H}^{\mathrm{vol}}$ denotes the contribution associated with the volumetric term $-(\Delta J - 1)\hat{\mu}/\upsilon$ and $\mathcal{H}^{\mathrm{mob}}$ denotes the contribution associated with solvent transport. The reciprocal relation between the standard off-diagonal linearizations is then preserved, i.e., $\mathbf{D}_{\mathbf{u}}\mathcal{H}^{\mathrm{vol}}(\mathbf{u}, \mu; \hat{\mu})[\Delta\mathbf{u}] = \mathbf{D}_{\mu}\mathcal{G}(\mathbf{u}, \mu; \Delta\mathbf{u})[\hat{\mu}]$. In contrast, retaining the full mobility tensor $\mathbf{M}_n = m_n(\mathbf{F}_n)(\Delta\mathbf{F}^T \Delta\mathbf{F})^{-1}$ introduces an additional contribution through $\mathbf{D}_{\mathbf{u}}\mathcal{H}^{\mathrm{mob}}(\mathbf{u}, \mu; \hat{\mu})[\Delta\mathbf{u}]$ that has no reciprocal counterpart in $\mathbf{D}_{\mu}\mathcal{G}(\mathbf{u}, \mu; \Delta\mathbf{u})[\hat{\mu}]$. Consequently, the reciprocal relation between the coupled linearizations is no longer satisfied, and the consistent tangent generally becomes unsymmetric. The adopted approximation therefore yields a reduced potential-energy functional with the symmetric mixed saddle-point structure required for the eigenvalue- and inertia-based stability analyses discussed in Section 3.6, consistent with the formulations of [71,73]. A formulation retaining the full incremental-deformation-dependence of the mobility would require a stability framework for asymmetric operators and represent a substantial extension beyond the scope of the present work.

3. Computational framework

In this section, we present the computational framework used to solve the mixed $\mathbf{u} - \mu$ problem of Section 2. We first augment the weak form with Nitsche terms to weakly impose Dirichlet boundary conditions on immersed boundaries; the symmetric variant is adopted to retain a symmetric tangent. The nonlinear system is linearized and solved by a Newton–Raphson scheme for each time increment. Spatially, we employ the Material Point Method (MPM): unknowns are represented on a fixed Eulerian B-spline grid and integrated on Lagrangian material points. To ensure robustness near incompressibility and at cut cells, we use subdivision-stabilized B-spline spaces for an *inf–sup* stable $\mathbf{u}-\mu$ discretization together with extended B-splines to cure cut-cell ill-conditioning and suppress cell-crossing artifacts. We close this section by describing the stability assessment, based either on the smallest eigenvalues of the reduced (Schur-complement) stiffness or, equivalently, on the inertia (signature) of the full coupled tangent.

3.1. Essential boundary conditions

In mesh-based methods, essential (Dirichlet) boundary conditions are enforced strongly at nodal degrees of freedom. For this purpose, the test functions $\hat{\mathbf{u}}$ and $\hat{\mu}$ vanish on the Dirichlet boundary with prescribed displacement or chemical potential, and the surface integrals in Eqs. (26) and (31) are taken over the Neumann parts of the boundary only. However, MPM uses Lagrangian particles to represent the domain, requiring boundary conditions to be imposed in a weak sense. In our setting for MPM, essential boundary conditions are imposed weakly via Nitsche's method [24,58]. To preserve consistency and stability, the Nitsche formulation modifies the weak form by adding three types of terms on the Dirichlet boundary: (1) a penalty term to weakly enforce the constraint, (2) a consistency term to ensure agreement with the strong form, and (3) a symmetric or skew-symmetric stabilization term to improve the stability of the formulation. With these terms, the modified weak form becomes:

$$\begin{aligned}
\mathcal{G}_{\mathrm{Nitsche}}(\mathbf{u}, \mu; \hat{\mathbf{u}}) &= \mathcal{G}(\mathbf{u}, \mu; \hat{\mathbf{u}}) + \underbrace{\beta_u \int_{\partial\Omega_n^{\mathbf{u}}} (\mathbf{u} - \overline{\mathbf{u}}) \cdot \hat{\mathbf{u}} \, \mathrm{d}A_n}_{\mathbf{u}\text{: Penalty term}} - \underbrace{s_u \int_{\partial\Omega_n^{\mathbf{u}}} (\mathbf{u} - \overline{\mathbf{u}}) \cdot \left(\frac{\partial \mathbf{P}_n}{\partial \Delta\mathbf{F}} : \boldsymbol{\nabla}_n \hat{\mathbf{u}} \right) \mathbf{N}_n \mathrm{d}A_n}_{\mathbf{u}\text{: Symmetry term}} \\
\mathcal{H}_{\mathrm{Nitsche}}(\mathbf{u}, \mu; \hat{\mu}) &= \mathcal{H}(\mathbf{u}, \mu; \hat{\mu}) - \underbrace{s_u \int_{\partial\Omega_n^{\mathbf{u}}} (\mathbf{u} - \overline{\mathbf{u}}) \cdot \left(\frac{\partial \mathbf{P}_n}{\partial \mu} \hat{\mu} \right) \mathbf{N}_n \mathrm{d}A_n}_{\mathbf{u}\text{: Symmetry term}} \\
&\quad - \underbrace{\beta_\mu \int_{\partial\Omega_n^{\mu}} \Delta t (\mu - \bar{\mu}) \hat{\mu} \mathrm{d}A_n}_{\mu\text{: Penalty term}} - \underbrace{s_\mu \int_{\partial\Omega_n^{\mu}} \Delta t \, m_n \boldsymbol{\nabla}_n \hat{\mu} \cdot \mathbf{N}_n (\mu - \bar{\mu}) \mathrm{d}A_n}_{\mu\text{: Symmetry term}}
\end{aligned} \tag{32}$$

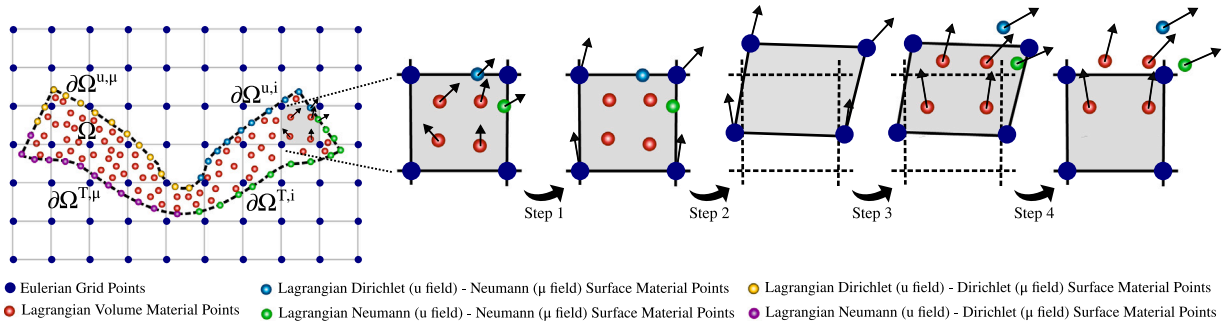

Fig. 2. (a) Discretization of the domain with Lagrangian material points within a stationary Eulerian grid. Separate sets of surface particles represent the combination of Dirichlet and Neumann boundaries for two fields $\mathbf{u}, \mu$. **(b)** The MPM workflow includes: (1) particle-to-grid mapping, (2) solution of governing equations on the grid, (3) transfer of updated fields back to the particles, and (4) resetting of the grid.

where $\bar{\mathbf{u}}$ is the prescribed displacement on the Dirichlet boundary $\partial\Omega_n^{\mathbf{u}}$ and $\bar{\mu}$ is the prescribed chemical potential on $\partial\Omega_n^{\mu}$. The consistent terms are included in the surface integrals over the entire boundary $\partial\Omega_n$ for $\mathcal{G}(\mathbf{u}, \mu; \hat{\mathbf{u}})$ and $\mathcal{H}(\mathbf{u}, \mu; \hat{\mu})$, whereas the penalty and symmetry terms integrate over the Dirichlet boundaries $\partial\Omega_n^{\mathbf{u}}, \partial\Omega_n^{\mu}$ only. For the penalty terms, $\beta_u = \gamma_u (N k_B T)/h_u$ and $\beta_\mu = \gamma_\mu m_n / h_\mu$, where γ_u and γ_μ are penalty factors, and h_u and h_μ are the grid spacings for discretization of displacement and chemical potential, respectively. For the symmetry terms, s_u and s_μ determine the symmetry of the formulation, similar to those terms derived previously for a mixed $\mathbf{u} - p$ formulation for incompressible hyperelasticity [24]. Although the skew-symmetric choice ($s_u = s_\mu = -1$) often exhibits unconditional coercivity for any $\gamma_u, \gamma_\mu > 0$, we adopt the symmetric variant ($s_u = s_\mu = 1$) in this work to retain a symmetric discrete tangent, which is convenient for the eigenvalue-based stability analysis in Section 3.6. The corresponding boundary integrals in Eq. (32) are evaluated using the surface material points associated with the prescribed displacement and chemical-potential boundaries, as described in Section 3.2, and are assembled into the global residual and tangent matrices without directly constraining the background-grid degrees of freedom.

3.2. Discretization using the material point method

The governing equations are solved using the material point method, a hybrid numerical approach that integrates features of both Eulerian and Lagrangian formulations. MPM operates on a stationary background grid — Eulerian in nature — whose nodes serve as degrees of freedom for solving the governing equations, such as momentum conservation (Eq. (26)) and mass conservation (Eq. (31)). Meanwhile, the actual physical domain Ω_0 is discretized by a collection of Lagrangian particles, which act as integration points. These particles move inside the stationary grid, and unlike standard Gauss points in finite element methods, they may traverse across elements during the simulation and form Ω_n.

The overall MPM algorithm can be broken down into four core stages, as illustrated in Fig. 2:

1. **Particle-to-grid (P2G) transfer:** Material point data are projected onto the grid nodes.
2. **Grid evolution:** The coupled equations are solved on the grid using the Newton–Raphson iterative algorithm in Section 3.3 to update nodal displacements and chemical potential.
3. **Grid-to-particle (G2P) transfer:** Updated grid quantities are interpolated back to the material points.
4. **Grid reset:** The computational grid is cleared and returned to its reference configuration in preparation for the next time step.

To accurately evaluate volume and surface integrals within the MPM framework, we categorize material points into five distinct types:

- *Volume points*: Used to discretize the bulk domain, each point is assigned a scalar volume V_p.
- *Dirichlet–Dirichlet boundary points*: Located on surfaces where both displacement ($\mathbf{u}$) and chemical potential (μ) are prescribed.
- *Dirichlet–Neumann boundary points*: Positioned on boundaries with prescribed displacement ($\mathbf{u}$) and solvent flux (Neumann condition on μ).
- *Neumann–Dirichlet boundary points*: Assigned to surfaces where traction (Neumann condition on $\mathbf{u}$) and chemical potential (μ) are specified.
- *Neumann–Neumann boundary points*: Represent surfaces with both traction and solvent flux boundary conditions.

Each of the four surface point types carries a vector quantity $\mathbf{N}_p A_p$, representing the directional area associated with that particle.

The spatial integrals are evaluated by summing over these particles:

$$\int_{\Omega_n} f(\mathbf{x})\,\mathrm{d}V_n \approx \sum_p f(\mathbf{x}_p)V_n(\mathbf{x}_p), \quad \int_{\partial\Omega_n} f(\mathbf{x})\,\mathrm{d}A_n \approx \sum_p f(\mathbf{x}_p)A_n(\mathbf{x}_p),$$
$$\int_{\partial\Omega_n} \mathbf{G}(\mathbf{x})\cdot\mathbf{N}_n\,\mathrm{d}A_n \approx \sum_p \mathbf{G}(\mathbf{x}_p)\cdot\mathbf{N}_n(\mathbf{x}_p)A_n(\mathbf{x}_p), \tag{33}$$

where $f(\mathbf{x})$ and $\mathbf{G}(\mathbf{x})$ are scalar and vector-valued functions, respectively. The particle volumes and areas are updated using:

$$V_n(\mathbf{x}_p) = J_n(\mathbf{x}_p)V_0(\mathbf{x}_p), \quad \mathbf{N}_n(\mathbf{x}_p)A_n(\mathbf{x}_p) = J_n(\mathbf{x}_p)\mathbf{F}_n^{-T}(\mathbf{x}_p)\mathbf{N}_0(\mathbf{x}_p)A_0(\mathbf{x}_p), \tag{34}$$

Here, $V_n(\mathbf{x}_p)$ and $\mathbf{N}_n(\mathbf{x}_p)A_n(\mathbf{x}_p)$ denote the volume and oriented surface area associated with a material point in the previously converged configuration, while $V_0(\mathbf{x}_p)$ and $\mathbf{N}_0(\mathbf{x}_p)A_0(\mathbf{x}_p)$ represent the corresponding quantities in the initial configuration.

3.3. Discretized Newton–raphson iterative scheme

The nonlinear coupled system in Eq. (32) at time $t_{n+1} = t_n + \Delta t$ is solved using a monolithic Newton–Raphson method. Let $(\mathbf{u}_{n+1}^k, \mu_{n+1}^k)$ denote the approximation of the solution at time t_{n+1} and Newton iteration k. The iterations are initialized from the converged solution at the previous time step,

$$\mathbf{u}_{n+1}^0 = \mathbf{u}_n, \qquad \mu_{n+1}^0 = \mu_n. \tag{35}$$

At iteration k+1, the unknowns are written in terms of the increments $\Delta\mathbf{u}_{n+1}^k$ and $\Delta\mu_{n+1}^k$ as

$$\mathbf{u}_{n+1}^{k+1} = \mathbf{u}_{n+1}^k + \Delta\mathbf{u}_{n+1}^k, \qquad \mu_{n+1}^{k+1} = \mu_{n+1}^k + \Delta\mu_{n+1}^k. \tag{36}$$

A first-order Taylor expansion of the residual functionals $\mathcal{G}_{\text{Nitsche}}$ and $\mathcal{H}_{\text{Nitsche}}$ about $(\mathbf{u}_{n+1}^k, \mu_{n+1}^k)$ yields

$$\begin{aligned}
\mathcal{G}_{\text{Nitsche}}(\mathbf{u}_{n+1}^{k+1}, \mu_{n+1}^{k+1}; \hat{\mathbf{u}}) &\approx \mathcal{G}_{\text{Nitsche}}(\mathbf{u}_{n+1}^k, \mu_{n+1}^k; \hat{\mathbf{u}}) \\
&\quad + \mathbf{D}_{\mathbf{u}}\mathcal{G}_{\text{Nitsche}}(\mathbf{u}_{n+1}^k, \mu_{n+1}^k; \hat{\mathbf{u}})[\Delta\mathbf{u}_{n+1}^k] \\
&\quad + \mathbf{D}_{\mu}\mathcal{G}_{\text{Nitsche}}(\mathbf{u}_{n+1}^k, \mu_{n+1}^k; \hat{\mathbf{u}})[\Delta\mu_{n+1}^k] \overset{!}{=} 0, \\
\mathcal{H}_{\text{Nitsche}}(\mathbf{u}_{n+1}^{k+1}, \mu_{n+1}^{k+1}; \hat{\mu}) &\approx \mathcal{H}_{\text{Nitsche}}(\mathbf{u}_{n+1}^k, \mu_{n+1}^k; \hat{\mu}) \\
&\quad + \mathbf{D}_{\mathbf{u}}\mathcal{H}_{\text{Nitsche}}(\mathbf{u}_{n+1}^k, \mu_{n+1}^k; \hat{\mu})[\Delta\mathbf{u}_{n+1}^k] \\
&\quad + \mathbf{D}_{\mu}\mathcal{H}_{\text{Nitsche}}(\mathbf{u}_{n+1}^k, \mu_{n+1}^k; \hat{\mu})[\Delta\mu_{n+1}^k] \overset{!}{=} 0.
\end{aligned} \tag{37}$$

Displacement and chemical potential fields are interpolated using separate shape functions associated with the grid nodes:

$$\begin{aligned}
\mathbf{u}(\mathbf{x}) &= \sum_{I=1}^{n_{\text{Nodes}}} N_I^{(u)}(\mathbf{x})\,\bar{\mathbf{u}}_I, \quad \mu(\mathbf{x}) = \sum_{I=1}^{n_{\text{Nodes}}} N_I^{(\mu)}(\mathbf{x})\,\bar{\mu}_I, \\
\hat{\mathbf{u}}(\mathbf{x}) &= \sum_{I=1}^{n_{\text{Nodes}}} N_I^{(u)}(\mathbf{x})\,\bar{\hat{\mathbf{u}}}_I, \quad \hat{\mu}(\mathbf{x}) = \sum_{I=1}^{n_{\text{Nodes}}} N_I^{(\mu)}(\mathbf{x})\,\bar{\hat{\mu}}_I.
\end{aligned} \tag{38}$$

where $\bar{\mathbf{u}}_I$ and $\bar{\mu}_I$ are the nodal coefficients of the trial fields $\mathbf{u}$ and μ, and $\bar{\hat{\mathbf{u}}}_I$ and $\bar{\hat{\mu}}_I$ are the nodal coefficients of the corresponding test functions $\hat{\mathbf{u}}$ and $\hat{\mu}$.

At time step t_{n+1} and Newton iteration k, the corresponding nodal coefficient vectors are denoted $\bar{\mathbf{u}}_{n+1}^k$ and $\bar{\mu}_{n+1}^k$. Inserting the discrete fields into the linearized weak forms at $(\mathbf{u}_{n+1}^k, \mu_{n+1}^k)$ yields the Newton system

$$\underbrace{\begin{bmatrix} \mathbf{K}_{uu}(\bar{\mathbf{u}}_{n+1}^k, \bar{\mu}_{n+1}^k) & \mathbf{K}_{u\mu}(\bar{\mathbf{u}}_{n+1}^k, \bar{\mu}_{n+1}^k) \\ \mathbf{K}_{\mu u}(\bar{\mathbf{u}}_{n+1}^k, \bar{\mu}_{n+1}^k) & \mathbf{K}_{\mu\mu}(\bar{\mathbf{u}}_{n+1}^k, \bar{\mu}_{n+1}^k) \end{bmatrix}}_{\text{Stiffness matrix}} \overbrace{\begin{bmatrix} \Delta\bar{\mathbf{u}}_{n+1}^k \\ \Delta\bar{\mu}_{n+1}^k \end{bmatrix}}^{\text{Incremental solution}} = -\underbrace{\begin{bmatrix} \mathbf{R}_u(\bar{\mathbf{u}}_{n+1}^k, \bar{\mu}_{n+1}^k) \\ \mathbf{R}_\mu(\bar{\mathbf{u}}_{n+1}^k, \bar{\mu}_{n+1}^k) \end{bmatrix}}_{\text{Residual vector}}, \tag{39}$$

where all residuals and tangent matrices are evaluated at the current iterate $(\mathbf{u}_{n+1}^k, \mu_{n+1}^k)$. More precisely, the residual functionals and their linearizations can be written as

$$\begin{aligned}
&\mathcal{G}_{\text{Nitsche}}(\mathbf{u}_{n+1}^k, \mu_{n+1}^k; \hat{\mathbf{u}}) = \bar{\hat{\mathbf{u}}}^{\mathrm{T}}\mathbf{R}_u(\bar{\mathbf{u}}_{n+1}^k, \bar{\mu}_{n+1}^k), \\
&\mathcal{H}_{\text{Nitsche}}(\mathbf{u}_{n+1}^k, \mu_{n+1}^k; \hat{\mu}) = \bar{\hat{\mu}}^{\mathrm{T}}\mathbf{R}_\mu(\bar{\mathbf{u}}_{n+1}^k, \bar{\mu}_{n+1}^k), \\
&\mathbf{D}_{\mathbf{u}}\mathcal{G}_{\text{Nitsche}}(\mathbf{u}_{n+1}^k, \mu_{n+1}^k; \hat{\mathbf{u}})[\Delta\mathbf{u}_{n+1}^k] = \bar{\hat{\mathbf{u}}}^{\mathrm{T}}\mathbf{K}_{uu}(\bar{\mathbf{u}}_{n+1}^k, \bar{\mu}_{n+1}^k)\,\Delta\bar{\mathbf{u}}_{n+1}^k, \\
&\mathbf{D}_{\mu}\mathcal{H}_{\text{Nitsche}}(\mathbf{u}_{n+1}^k, \mu_{n+1}^k; \hat{\mu})[\Delta\mu_{n+1}^k] = \bar{\hat{\mu}}^{\mathrm{T}}\mathbf{K}_{\mu\mu}(\bar{\mathbf{u}}_{n+1}^k, \bar{\mu}_{n+1}^k)\,\Delta\bar{\mu}_{n+1}^k, \\
&\mathbf{D}_{\mu}\mathcal{G}_{\text{Nitsche}}(\mathbf{u}_{n+1}^k, \mu_{n+1}^k; \hat{\mathbf{u}})[\Delta\mu_{n+1}^k] = \bar{\hat{\mathbf{u}}}^{\mathrm{T}}\mathbf{K}_{u\mu}(\bar{\mathbf{u}}_{n+1}^k, \bar{\mu}_{n+1}^k)\,\Delta\bar{\mu}_{n+1}^k, \\
&\mathbf{D}_{\mathbf{u}}\mathcal{H}_{\text{Nitsche}}(\mathbf{u}_{n+1}^k, \mu_{n+1}^k; \hat{\mu})[\Delta\mathbf{u}_{n+1}^k] = \bar{\hat{\mu}}^{\mathrm{T}}\mathbf{K}_{\mu u}(\bar{\mathbf{u}}_{n+1}^k, \bar{\mu}_{n+1}^k)\,\Delta\bar{\mathbf{u}}_{n+1}^k.
\end{aligned} \tag{40}$$

3.4. Subdivision B-spline shape functions

We now provide a brief overview of the construction of subdivision B-spline basis functions used to discretize the displacement and chemical potential fields, designed to ensure numerical stability in the mixed formulation.

B-spline functions of degree q are defined over a non-decreasing knot vector $\Xi = [\xi_1, \xi_2, \dots, \xi_{n+q+1}]$, where n denotes the number of basis functions. The basis functions are constructed recursively using the Cox–de Boor formula [82], beginning with:

$$N_{i,0}(\xi) = \begin{cases} 1 & \text{if } \xi_i \le \xi < \xi_{i+1}, \\ 0 & \text{otherwise.} \end{cases} \tag{41}$$

For degrees $q \ge 1$, the recursion proceeds as:

$$N_{i,q}(\xi) = \frac{\xi - \xi_i}{\xi_{i+q} - \xi_i} N_{i,q-1}(\xi) + \frac{\xi_{i+q+1} - \xi}{\xi_{i+q+1} - \xi_{i+1}} N_{i+1,q-1}(\xi), \tag{42}$$

where $N_{i,q}(\xi)$ is the ith basis function evaluated at parametric coordinate ξ; terms with zero denominators are taken to be zero. These functions form a partition of unity on the parametric domain, i.e., $\sum_i N_{i,q}(\xi) = 1$.

To construct a d-dimensional tensor-product B-spline volume embedded in $\mathbb{R}^{d_s}$, $d \le d_s \le 3$, we employ a tensor-product basis on the parametric domain $\hat{\Omega} \subset \mathbb{R}^d$. For a parametric coordinate $\boldsymbol{\xi} = (\xi_1, \xi_2, \dots, \xi_d) \in \hat{\Omega}$, we define the geometry mapping $\mathbf{x} = C_{dD}^{(q_1,\dots,q_d)} : \hat{\Omega} \to \bar{\Omega} \subset \mathbb{R}^{d_s}$ by the control points $\mathbf{B}_{i_1,i_2,\dots,i_d} \in \mathbb{R}^{d_s}$ as

$$C_{dD}^{(q_1,q_2,\dots,q_d)}(\boldsymbol{\xi}) = \sum_{i_1=1}^{n_1} \cdots \sum_{i_d=1}^{n_d} \left[\prod_{j=1}^{d} N_{i_j,q_j}(\xi_j) \right] \mathbf{B}_{i_1,\dots,i_d} \in \mathbb{R}^{d_s}, \tag{43}$$

where $N_{i_j,q_j}(\xi_j)$ denotes the univariate B-spline basis function of degree q_j in the jth parametric direction, and n_j is the number of basis functions (equivalently, control points) in that direction. Equivalently, introducing the multi-index $\boldsymbol{i} = (i_1, \dots, i_d)$ with $i_\alpha \in \{1, \dots, n_\alpha\}$ and $\boldsymbol{q} = (q_1, \dots, q_d)$, and defining the tensor-product basis

$$N_{\boldsymbol{i},\boldsymbol{q}}(\boldsymbol{\xi}) := \prod_{\alpha=1}^{d} N_{i_\alpha,q_\alpha}(\xi_\alpha), \tag{44}$$

the mapping can be written compactly as

$$C_{dD}^{(q)}(\boldsymbol{\xi}) = \sum_{\boldsymbol{i}} N_{\boldsymbol{i},\boldsymbol{q}}(\boldsymbol{\xi}) \mathbf{B}_{\boldsymbol{i}}, \qquad \sum_{\boldsymbol{i}} := \sum_{i_1=1}^{n_1} \cdots \sum_{i_d=1}^{n_d}, \tag{45}$$

where $\mathbf{B}_{\boldsymbol{i}} \equiv \mathbf{B}_{i_1,\dots,i_d} \in \mathbb{R}^{d_s}$.

Following Ali Madadi and Dortdivanlioglu [24,72], we construct a d-dimensional tensor-product B-spline grid of degree q on $\hat{\Omega} = [0, L_1] \times [0, L_2] \dots \times [0, L_d]$ with uniform interior knot spacing (open knot vectors). The associated control points are chosen so that the geometry mapping is the identity on $\hat{\Omega}$ (i.e., $\mathbf{x}(\boldsymbol{\xi}) = \boldsymbol{\xi}$), and therefore the parametric and physical domains coincide.

To satisfy the *inf–sup* condition in mixed formulations, we exploit the hierarchical (two-scale) refinement property of tensor-product B-splines. In this strategy, the chemical potential field is interpolated on a coarse grid (cell size 2 h), while the displacement field is interpolated on a refined grid (cell size h) obtained by uniform dyadic knot refinement.

Let q denote the (common) spline degree in each parametric direction. We denote by $N_{i_\alpha,q}^{(u)}(\xi_\alpha)$ and $N_{i_\alpha,q}^{(\mu)}(\xi_\alpha)$ the univariate B-spline basis functions on the fine and coarse knot vectors, respectively, along direction $\alpha = 1, \dots, d$. For uniform dyadic refinement, each coarse univariate basis function can be written exactly as a linear combination of fine basis functions,

$$N_{i,q}^{(\mu)}(\xi) = \sum_{k=0}^{q+1} a_k^{(q)} N_{2i+k-1,q}^{(u)}(\xi), \qquad a_k^{(q)} = \frac{1}{2^q} \binom{q+1}{k}, \tag{46}$$

where $\{a_k^{(q)}\}_{k=0}^{q+1}$ is the degree-q refinement mask.

Using the multi-index notation introduced above and Eq. (44), and noting that here $q_\alpha = q$, let $\boldsymbol{i} = (i_1, \dots, i_d)$ and $\boldsymbol{k} = (k_1, \dots, k_d)$. Taking tensor products of Eq. (46) yields the d-dimensional refinement relation

$$N_{i,q}^{(\mu)}(\boldsymbol{\xi}) = \prod_{\alpha=1}^{d} \left(\sum_{k_\alpha=0}^{q+1} a_{k_\alpha}^{(q)} N_{2i_\alpha+k_\alpha-1,q}^{(u)}(\xi_\alpha) \right) = \sum_{k_1=0}^{q+1} \cdots \sum_{k_d=0}^{q+1} \left(\prod_{\alpha=1}^{d} a_{k_\alpha}^{(q)} \right) N_{2\boldsymbol{i}+\boldsymbol{k}-\mathbf{1},q}^{(u)}(\boldsymbol{\xi}), \tag{47}$$

where $\mathbf{1} = (1, \dots, 1)$.

In matrix form, let $\mathbf{N}^{(u)}(\boldsymbol{\xi})$ and $\mathbf{N}^{(\mu)}(\boldsymbol{\xi})$ collect the fine- and coarse-grid tensor-product basis functions, respectively. Let $\mathbf{S}^{(q)}$ denote the (banded) *univariate* refinement operator induced by the mask $a_k^{(q)}$ in Eq. (46). Then the d-dimensional refinement operator is the tensor-product (Kronecker) product

$$\mathbf{N}^{(\mu)}(\boldsymbol{\xi}) = \mathbf{S}_{dD}^{(q)} \mathbf{N}^{(u)}(\boldsymbol{\xi}), \qquad \mathbf{S}_{dD}^{(q)} = \underbrace{\mathbf{S}^{(q)} \otimes \cdots \otimes \mathbf{S}^{(q)}}_{d \text{ times}}. \tag{48}$$

For reference, the refinement masks (and hence the nonzero bands of $\mathbf{S}^{(q)}$) for $q = 1, 2, 3$ are

$$a^{(1)} = \tfrac{1}{2}[1, 2, 1], \qquad a^{(2)} = \tfrac{1}{4}[1, 3, 3, 1], \qquad a^{(3)} = \tfrac{1}{8}[1, 4, 6, 4, 1]. \tag{49}$$

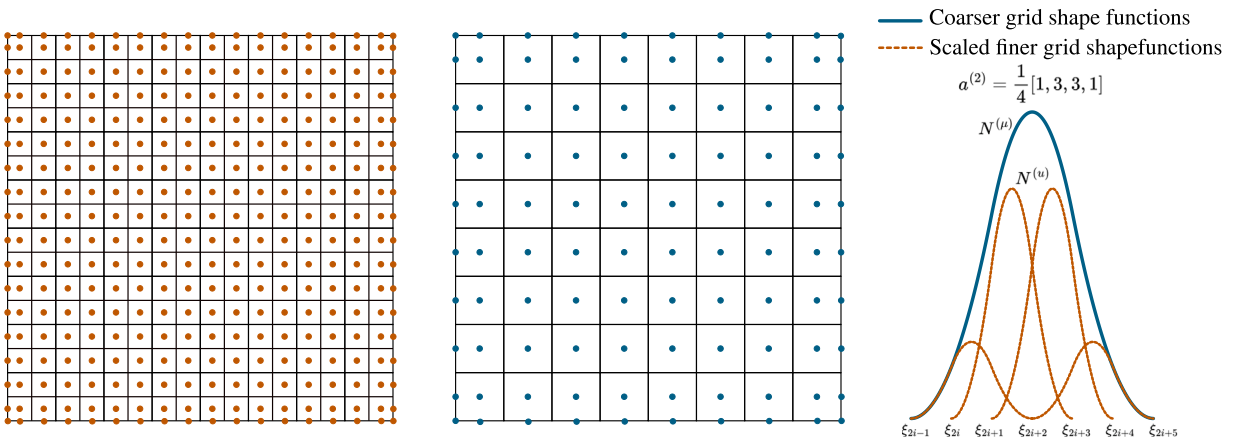

(a) Finer scale grid (b) Coarser scale grid (c) Quadratic subdivision matrix

Fig. 3. Illustration of the subdivision-stabilized B-spline construction for quadratic shape functions: the chemical potential is discretized on a coarse grid (spacing $2h$), while displacement is discretized on the refined grid (spacing h) obtained by uniform dyadic knot refinement.

A schematic illustration of the two grids used for discretizing the displacement and chemical potential fields, together with the associated subdivision relation, is shown in Fig. 3.

3.5. Cut-cell instability

This section outlines our strategy for resolving cut-cell instability, which stems from the ill-conditioning of the stiffness matrix due to the presence of partially filled boundary grid cells.

One efficient approach to resolve this issue is to use the extended B-splines approach [39,63] to transfer the contribution of the boundary nodal points to the interior ones. To this end, we should categorize each field's grid cells into interior, boundary, and outer cells. The outer cells are those without any physical material points, whereas any cell with material points that has an outer cell as its neighbor is called a boundary grid cell. The rest of the cells are called interior ones. Similarly, we categorize the control points in both displacement and chemical potential grids into interior, boundary, and outer ones based on the support of the B-spline function related to each control point over grid cells. If this support has at least one interior grid cell, the control point is assigned as an interior one. If the support contains a boundary grid cell and no interior one, the control point is set as a boundary one. The rest of the control points are considered to be outer ones. For a d-dimensional problem using B-splines of degree q in all directions, let $\mathcal{A} \in \{\mathbf{u}, \mu\}$ denote a generic field. We split the control points into interior indices $\mathcal{I}$ and boundary indices $\mathcal{B}$ and write

$$\mathcal{A}(\mathbf{x}) = \sum_{i \in \mathcal{I}} N_{i,q}^{(\mathcal{A})}(\mathbf{x})\, \mathcal{A}_i + \sum_{k \in \mathcal{B}} N_{k,q}^{(\mathcal{A})}(\mathbf{x})\, \mathcal{A}_k. \tag{50}$$

Each boundary degree of freedom $\boldsymbol{k}$ is extrapolated from the nearest neighboring block of $(q+1)^d$ interior indices:

$$\mathcal{A}_{\boldsymbol{k}} = \sum_{i \in \mathcal{I}_{\boldsymbol{k}}} E_{i\boldsymbol{k}}\, \mathcal{A}_i, \qquad \boldsymbol{k} \in \mathcal{B}. \tag{51}$$

Here, $\mathcal{I}_{\boldsymbol{k}} \subset \mathcal{I}$ denotes the nearest $(q+1)^d$ interior block associated with $\boldsymbol{k}$, with lower-corner index $\boldsymbol{l} = (l_1, \dots, l_d)$,

$$\mathcal{I}_{\boldsymbol{k}} = \{\boldsymbol{i} \in \mathcal{I} \mid l_\alpha \le i_\alpha \le l_\alpha + q,\ \alpha = 1, \dots, d\}. \tag{52}$$

Define the inverse incidence set $\mathcal{I}_i^{-1} := \{\, \boldsymbol{k} \in \mathcal{B} \mid \boldsymbol{i} \in \mathcal{I}_{\boldsymbol{k}} \,\}$. Substitution yields a representation involving only interior unknowns,

$$\mathcal{A}(\mathbf{x}) = \sum_{i \in \mathcal{I}} \tilde{N}_{i,q}^{(\mathcal{A})}(\mathbf{x})\, \mathcal{A}_i, \qquad \tilde{N}_{i,q}^{(\mathcal{A})}(\mathbf{x}) = N_{i,q}^{(\mathcal{A})}(\mathbf{x}) + \sum_{k \in \mathcal{I}_i^{-1}} E_{i\boldsymbol{k}}\, N_{k,q}^{(\mathcal{A})}(\mathbf{x}). \tag{53}$$

The Lagrange polynomial coefficients $E_{i\boldsymbol{k}}$ are computed by tensor-product Lagrange interpolation over the selected interior block $\mathcal{I}_{\boldsymbol{k}}$:

$$E_{i\boldsymbol{k}} = \prod_{\alpha=1}^{d} \left(\prod_{\substack{s_\alpha = l_\alpha \\ s_\alpha \neq i_\alpha}}^{l_\alpha + q} \frac{k_\alpha - s_\alpha}{i_\alpha - s_\alpha} \right), \qquad \boldsymbol{i} \in \mathcal{I}_{\boldsymbol{k}}. \tag{54}$$

A schematic illustration of the grid-cell and control-point categorization, along with the corresponding coefficients in Eq. (54), for quadratic B-splines is shown in Fig. 4.

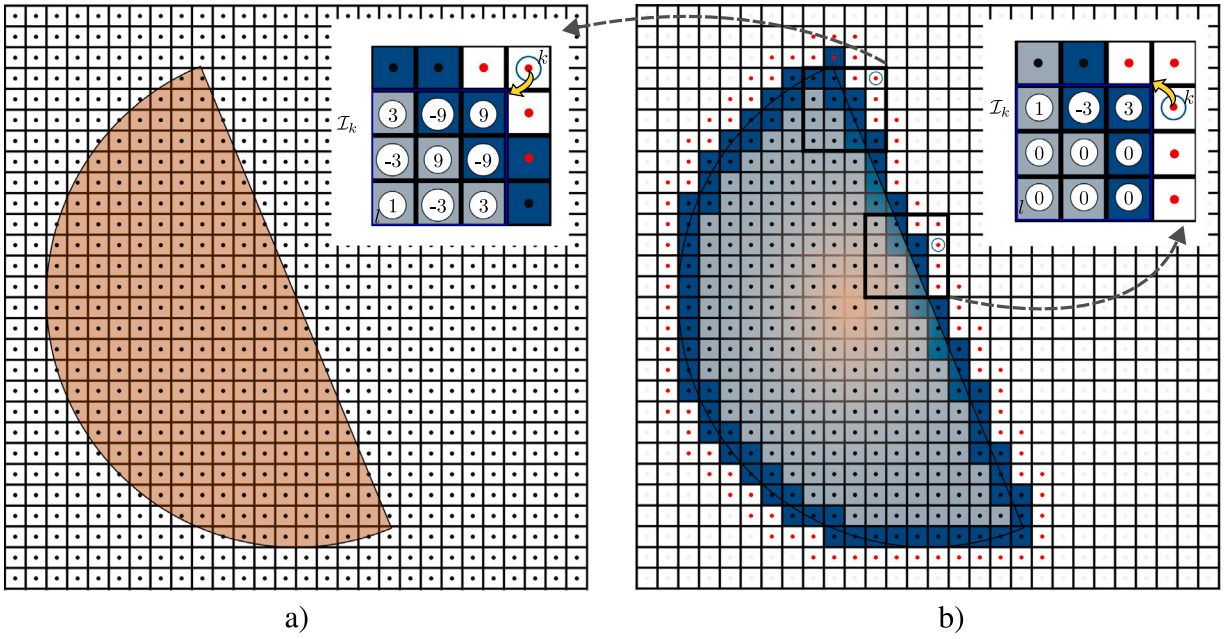

Fig. 4. Schematic illustration of the extended B-spline strategy near boundaries. **(a)** The computational domain. **(b)** Classification of grid cells and control points: blue cells represent boundary grid cells, white cells are exterior (inactive) regions, and light blue cells denote interior grid cells. Black dots indicate interior control points, while red dots mark boundary control points. For each field, the value at a boundary control point is extrapolated from a surrounding block of interior control points using Lagrange polynomials. Insets in (a) and (b) show the extrapolation coefficients associated with this process.

For example, consider a one-dimensional quadratic basis ($q = 2$), for which each boundary control point k is extrapolated from three consecutive interior control points. If the selected interior block lies immediately to the left of k, so that $\mathcal{I}_k = \{l, l+1, l+2\}$ with $l = k - 3$, direct evaluation of Eq. (54) gives $\left[E_{lk},\, E_{(l+1)k},\, E_{(l+2)k}\right] = [\,1, -3,\, 3\,]$. If the interior block lies to the right of the boundary control point, the corresponding coefficients are $[\,3, -3,\, 1\,]$. The resulting one-dimensional extension process is illustrated in Fig. 5 for the one-dimensional domain $x \leq 9.75$ with a uniform knot spacing of 0.5.

In two dimensions, the coefficients are obtained by the tensor product of the corresponding one-dimensional coefficient vectors. First, consider a boundary control point whose associated 3×3 interior block is adjacent to it in one coordinate direction and aligned with it in the other. In this case, one directional coefficient vector is $[\,3, -3,\, 1\,]$, while the aligned direction contributes $[\,1,\, 0,\, 0\,]$. Their tensor product gives

$$\begin{bmatrix} 1 \\ 0 \\ 0 \end{bmatrix} \begin{bmatrix} 3 & -3 & 1 \end{bmatrix} = \begin{bmatrix} 3 & -3 & 1 \\ 0 & 0 & 0 \\ 0 & 0 & 0 \end{bmatrix}, \tag{55}$$

up to the orientation of the selected interior block. Thus, only the row or column adjacent to the boundary control point contains nonzero coefficients.

Next, consider a boundary control point located diagonally from its associated 3×3 interior block. In this case, both directional coefficient vectors are nontrivial, and their tensor product gives

$$\begin{bmatrix} 1 \\ -3 \\ 3 \end{bmatrix} \begin{bmatrix} 3 & -3 & 1 \end{bmatrix} = \begin{bmatrix} 3 & -3 & 1 \\ -9 & 9 & -3 \\ 9 & -9 & 3 \end{bmatrix}. \tag{56}$$

The numerical values shown in the insets of Fig. 4 are precisely the coefficients E_{ik} obtained from Eq. (54) and arranged according to the locations of the corresponding interior control points. The remaining coefficient patterns follow analogously from the relative position and orientation of the boundary control point and its selected interior block.

The key idea behind extended B-splines is inspired by Marsden's theorem [68], which asserts that any polynomial of the form $(x - t)^q$ can be expressed as

$$(x-t)^q = \sum_{i \in \mathbb{Z}} \Psi^h_{i,q}\, N^h_{i,q}(x) \quad , \quad \Psi^h_{i,q} = h^q \left(i + 1 - \frac{t}{h}\right)\left(i + 2 - \frac{t}{h}\right) \cdots \left(i + q - \frac{t}{h}\right), \tag{57}$$

where $N^h_{i,q}(x)$ denotes the qth-degree B-spline basis function associated with the ith knot in a uniformly spaced knot vector with spacing h. Extending this idea to a d-dimensional setting by taking the product in each coordinate direction and using Eq. (44), we

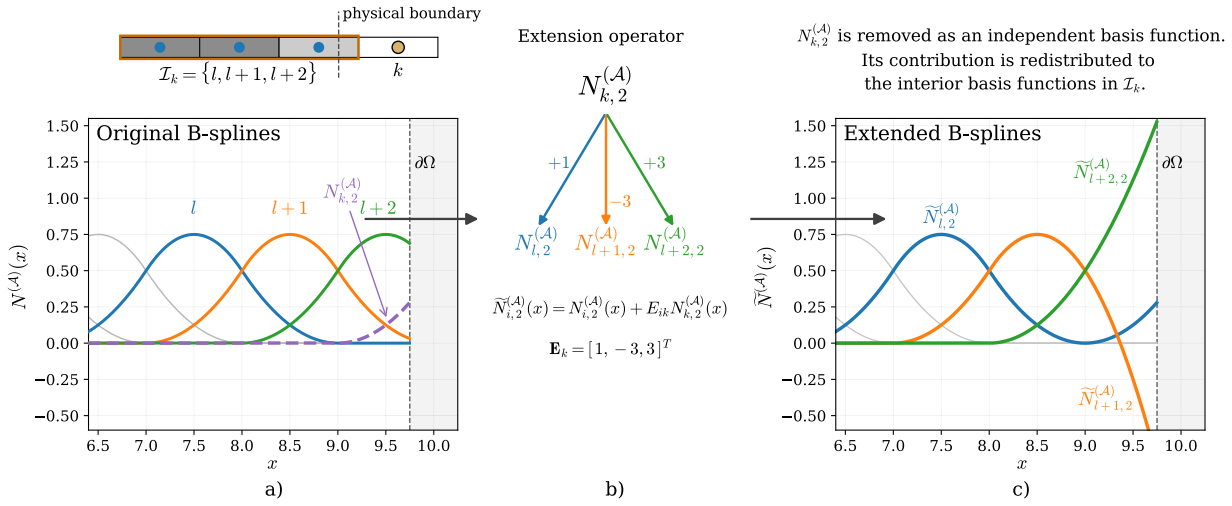

Fig. 5. One-dimensional illustration of the extended B-spline construction for a quadratic basis. (**a**) A boundary basis function $N_{k,2}^{(\mathcal{A})}$ is associated with the nearest interior block $\mathcal{I}_k = \{l, l+1, l+2\}$. (**b**) The extension operator redistributes the contribution of the boundary basis function to the three interior basis functions using the extrapolation coefficients $\mathbf{E}_k = [1, -3, 3]^T$ obtained from Eq. (54). (**c**) The resulting extended basis functions contain only interior degrees of freedom while preserving the contribution of the removed boundary basis function.

obtain:

$$\prod_{\alpha=1}^{d} \left(x_\alpha - t_\alpha\right)^q = \sum_{i \in \mathbb{Z}^d} w_q^h(\boldsymbol{i}, \boldsymbol{t})\, N_{i,q}(\mathbf{x}) \quad , \quad w_q^h(\boldsymbol{i}, \boldsymbol{t}) = \prod_{\alpha=1}^{d} \Psi_{i_\alpha,q}^h(t_\alpha). \tag{58}$$

By differentiating Eq. (58), r_α times with respect to t_α for each direction and subsequently setting $t_\alpha = 0$, one can show that any polynomial $p(\mathbf{x}) = \sum_{v \le q} c_v\, x^v$, can be written as a linear combination of B-spline shape functions over the domain $\bar{\Omega}$:

$$p(\mathbf{x}) = \sum_{i \in \mathcal{I} \cup \mathcal{B}} w(\boldsymbol{i})\, N_{i,q}(\mathbf{x}), \tag{59}$$

where $w(\boldsymbol{i})$ is a multivariate function that is a polynomial of order at most q in each variable. This expression can be partitioned into interior and boundary contributions:

$$p(\mathbf{x}) = \sum_{i \in \mathcal{I}} w(\boldsymbol{i})\, N_{i,q}(\mathbf{x}) + \sum_{k \in \mathcal{B}} w(\boldsymbol{k})\, N_{k,q}(\mathbf{x}). \tag{60}$$

Here, $w(\boldsymbol{k})$ is a polynomial of order at most q in each direction. Thus, $w(\boldsymbol{k})$ can be represented as a linear combination of the $w(\boldsymbol{i})$ values over a block of $(q+1)^d$ interior indices $(\mathcal{I}_{\boldsymbol{k}})$:

$$w(\boldsymbol{k}) = \sum_{i \in \mathcal{I}_{\boldsymbol{k}}} E_{i\boldsymbol{k}}\, w(\boldsymbol{i}). \tag{61}$$

Substituting this relation into Eq. (60), we obtain:

$$p(\mathbf{x}) = \sum_{i \in \mathcal{I}} w(\boldsymbol{i}) \underbrace{\left[N_{i,q}(\mathbf{x}) + \sum_{k \in \mathcal{I}_i^{-1}} E_{i\boldsymbol{k}}\, N_{k,q}(\mathbf{x}) \right]}_{\tilde{N}_{i,q}(\mathbf{x})}, \tag{62}$$

which is equivalent to the modified shape functions in Eq. (53). This modified basis preserves polynomial completeness and enables stable numerical solutions even in the presence of partially filled boundary cells.

3.6. Stability analysis

Referring back to Eq. (39), we follow the discussion in Dortdivanlioglu and Linder [15] to check the stability of the obtained solutions. Two equivalent methods can be used for this purpose. First, we can reduce Eq. (39) to a one-field displacement-based equation as follows:

$$\underbrace{\left(\mathbf{K}_{uu} - \mathbf{K}_{u\mu}\mathbf{K}_{\mu\mu}^{-1}\mathbf{K}_{\mu u}\right)}_{\mathbf{S}}\, \Delta\bar{\mathbf{u}} = \underbrace{\left(\mathbf{K}_{u\mu}\mathbf{K}_{\mu\mu}^{-1}\mathbf{R}_\mu - \mathbf{R}_u\right)}_{-\mathbf{R}_S}. \tag{63}$$

Table 1
Material and numerical parameters used in all simulations.

Shear modulus	Flory–Huggins parameter	Normalized solvent volume	Initial isotropic stretch	Initial chemical potential	Displacement penalty	Chemical potential penalty
Nk_BT	χ	Nv	λ_0	$\mu_0/(k_BT)$	γ_u	γ_μ
1.0 MPa	0.10	7.299×10^{-3}	1.2801	−0.1460	1000	25

Here, the matrix $\mathbf{S}$ is called the Schur complement of $\mathbf{K}_{uu}$ in $\mathbf{K}$ or the reduced stiffness matrix. Since both $\mathbf{K}_{uu}$ and $-\mathbf{K}_{\mu\mu}$ are positive definite in a structurally stable state, and $\mathbf{K}_{u\mu}=\mathbf{K}_{\mu u}^T$, $\mathbf{S}$ is also positive definite, and its eigenvalues should be real and positive. The drawback of this method is that computing the Schur complement is memory-intensive and inefficient.

Alternatively, we can track the signature of the stiffness matrix $\mathbf{K}$, defined as a three-component vector (n^+,n^-,n^0), where the components indicate the number of positive, negative, and zero eigenvalues, respectively. Assume $\mathbf{K}_{uu}$ and $\mathbf{K}_{\mu\mu}$ are the $n\times n$ and $m\times m$ matrices, respectively. Here, we use Sylvester's law of inertia [83], which states that matrix $\mathbf{K}$, and the diagonal matrix $\mathbf{D}$ in Cholesky's decomposition $\mathbf{K}=\boldsymbol{L}\mathbf{D}\boldsymbol{L}^T$, where $\boldsymbol{L}$ is a lower triangular unit matrix, have the same signature. Since $\mathbf{K}_{uu}$ and $\mathbf{K}_{\mu\mu}$ are positive and negative definite matrices, respectively, the matrix $\mathbf{K}$ should have n positive and m negative eigenvalues in a structurally stable state. Thus, its signature should be $(n,m,0)$. In both approaches, a bisection method can be used to track the smallest eigenvalue of $\mathbf{S}$ or the signature of $\mathbf{K}$ if an unstable solution is obtained. Due to the inherent perturbations in MPM, we do not expect to reach the exact onset of instability ($\lambda_{cr}=0$ or $n^0>0$) during the simulation, but we can simulate the pre- and post-instability behaviors as demonstrated by numerical examples in the next section.

4. Numerical examples

This section illustrates the accuracy and stability of the proposed framework through a sequence of numerical tests of increasing complexity. We begin with one-dimensional constrained swelling of a hydrogel layer and validate the MPM implementation against a semi-analytical solution. We then consider flat punch indentation of hydrogel as a benchmark problem, contrasting the instantaneous (undrained) response with the long-term (drained) behavior to illustrate the necessity of an *inf–sup* (LBB) stable $\mathbf{u}-\mu$ discretization during the initial loading stage. Finally, we demonstrate the capability of the proposed framework to simulate swelling-induced instabilities in two settings: (i) buckling of a constrained hydrogel column, and (ii) a symmetry-breaking bifurcation and subsequent surface creasing in a perforated gel with periodic cylindrical pores. In the numerical examples, we adopt the notation Qi to denote a quadrilateral discretization of order i with the highest possible continuity. For mixed formulations, Qi–Qj indicates that the displacement field is discretized with basis functions of order i, whereas the chemical potential field is discretized with basis functions of order j. If subdivision stabilization is used, the notation is written as Qi–QjSD, where 'SD' signifies that the chemical-potential field is discretized on a grid twice as coarse as the displacement grid through the subdivision construction, while the polynomial orders remain i and j for the displacement and chemical-potential fields, respectively. Except for the second example, where different discretizations are compared, the $Q2$–$Q2$SD discretization is used throughout. Across all numerical examples considered, the subdivision-stabilized extended B-spline bases together with symmetric Nitsche enforcement yield smooth, oscillation-free chemical-potential fields and well-conditioned tangents, enabling robust solutions and reliable stability diagnostics. All material and numerical parameters used in the simulations are listed in Table 1, except for μ_0 and λ_0 in Section 4.2, where we adopt a fully swollen initial configuration ($\mu_0=0$). For all simulations, we employ an adaptive implicit scheme for time integration in which the time step Δt is updated based on Newton–Raphson behavior: if the iterations fail to converge, we reduce the step size by setting $\Delta t\leftarrow\Delta t/2$; if convergence is achieved in fewer than six iterations, we increase it via $\Delta t\leftarrow 1.25\,\Delta t$.

4.1. Constrained one-dimensional swelling

In this example, we validate the proposed MPM formulation against the finite-difference (FDM) reference solution for constrained swelling of a hydrogel layer [13,81]. The layer is constrained in the in-plane directions and swells in the thickness (Y) direction. The deformation gradient takes the form $\mathbf{F}(Y,t)=\mathrm{diag}\big(\lambda_0,\lambda_0\lambda(Y,t),\lambda_0\big)$, where $\lambda_0>1$ is a homogeneous pre-stretch and $\lambda(Y,t)$ is the additional uniaxial stretch due to swelling in the thickness (Y) direction (see Fig. 6a). At $t=0$, the gel is taken to be stress-free with the pre-stretch λ_0 and the corresponding initial chemical potential μ_0 (see Table 1). As a reference, a nonlinear one-dimensional diffusion equation was derived and solved by FDM in Bouklas and Huang [81], by discretizing along the thickness direction (Y) in the reference configuration. The chemical potential at the top surface is prescribed as $\mu/(k_BT)=0$, while the no-flux condition is set at the bottom surface. From the resulting solution, the transient fields of chemical potential $\mu(Y,t)$ and stretch $\lambda(Y,t)$ are computed at each time step. The change of the layer thickness is then computed as a function of time, $\Delta h(t)=h(t)-h_0$, where the thickness $h(t)$ is calculated by integrating the stretch $\lambda(Y,t)$ over Y and $h_0=\lambda_0 H$. This FDM solution is used as the benchmark for the layer thickness evolution $\Delta h(t)/h_0$ and the chemical-potential profiles $\mu(Y,t)$ in Fig. 6(b–c). Moreover, a self-similar analytical solution was developed in Bouklas and Huang [81], which predicted that $\Delta h(t)\propto\sqrt{t}$ in the early stage of swelling.

To solve this problem using the material point method, we consider a 2D model of a hydrogel block immersed in a rectangular grid shown in Fig. 6a. The computational grid spans $0.5h_0\times 4h_0$, and the hydrogel block has dimensions $0.2h_0\times h_0$ in the initial configuration. The displacement field is discretized using a 20×160 quadratic grid, while a coarser 10×80 quadratic grid is

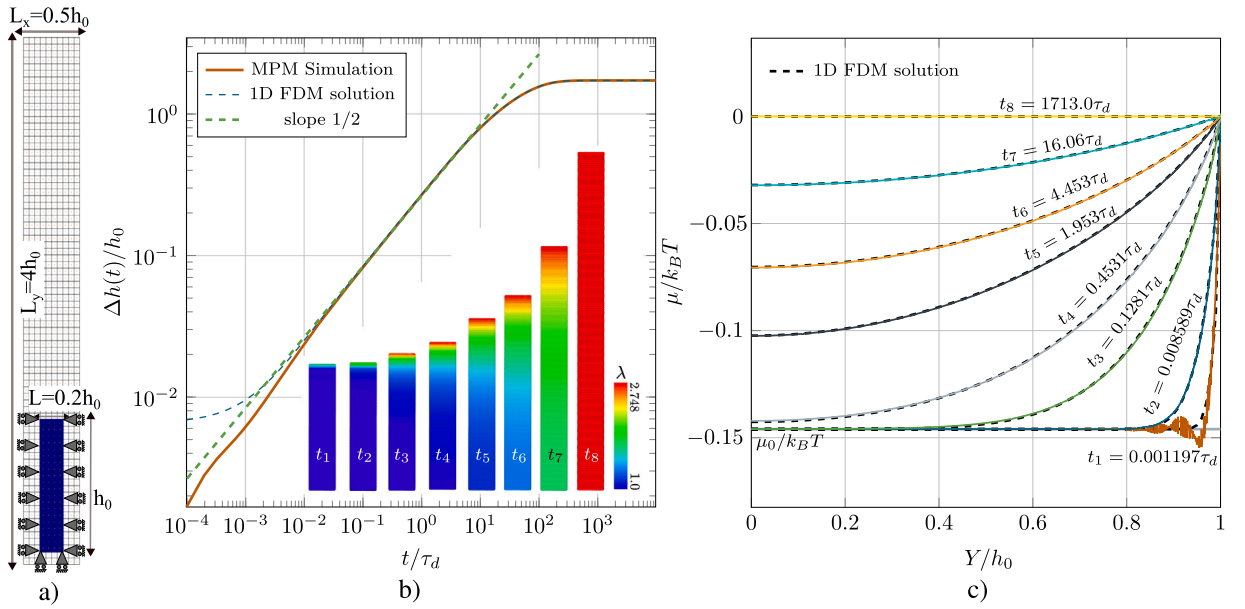

Fig. 6. (a) Schematic of the geometry and boundary conditions for simulating one-dimensional swelling of hydrogel. **(b)** Comparison of the normalized swelling-induced thickness change, $\Delta h(t)/h_0$, by the MPM implementation and the semi-analytical solution by finite difference (FDM). Overlaid contours display the spatial distribution of stretch λ at $t/\tau_d = 0.0011197$, 0.008589, 0.1281, 0.4531, 1.953, 4.453, 16.06, and 1713. The characteristic diffusion timescale based on the initial configuration is $\tau_d = h_0^2/D$. **(c)** Distribution profiles of the chemical potential over time obtained from MPM and FDM.

used for the chemical potential field. Each active cell within the block is discretized with 6×6 material points, corresponding to a total of 11,520 material points in 320 cells for the initial configuration. This relatively high density of material points in the initial configuration is used to maintain adequate quadrature resolution with sufficient density of material points in all active cells during swelling. A boundary condition of $\mu/(k_BT) = 0$ is instantly applied to the top surface at $t = 0^+$, and then maintained constant until the end of the simulation at $t_{\text{final}}/\tau_d = 1713$; all other boundaries are set to be impermeable (no flux). The characteristic diffusion timescale based on the initial configuration, $\tau_d = h_0^2/D$, is used to normalize the time. We impose an essential (symmetry) boundary condition $\mathbf{u} \cdot \mathbf{N}_n = 0$ on the left and right boundaries, and $\mathbf{u} = 0$ on the bottom boundary. On the top boundary, the traction-free condition is imposed. In addition, we enforce a constraint on the displacement in the tangential direction, $\mathbf{u} \cdot \mathbf{N}_n^{\perp} = 0$, to suppress potential surface instabilities [13]. For MPM simulations, the adaptive implicit time stepping starts with $\Delta t/\tau_d = 8.75 \times 10^{-5}$, and increases during the simulation. To maintain accuracy and limit the time step, we impose stage-wise caps on Δt as:

$$\Delta t/\tau_d \leq \begin{cases} 0.0125, & 0 \leq t/\tau_d \leq 5, \\ 0.0625, & 5 < t/\tau_d \leq 20, \\ 0.125, & 20 < t/\tau_d \leq 40, \\ 0.625, & 40 < t/\tau_d \leq 100. \end{cases} \tag{64}$$

Fig. 6b compares the normalized swelling-induced thickness change, $\Delta h(t)/h_0$, predicted by the MPM and the reference FDM solution. The two solutions are in close agreement overall, providing a validation of the MPM implementation. We also include the self-similar scaling, $\Delta h(t) \propto \sqrt{t}$, for comparison. In the instantaneous-loading limit, the analytical self-similar solution predicts $\Delta h(t) \propto \sqrt{Dt}$ as $t \to 0$ [81], corresponding to a slope of 0.5 on a log–log plot. At very early times, the FDM solution shows a slight deviation from this self-similar behavior, consistent with previous finite-difference and finite element studies of the same problem [13,81], where the discrepancy was attributed to the abrupt step change in surface chemical potential at $t = 0^+$ and the resulting thin diffusive boundary layer. By contrast, the closer agreement of the MPM result with the self-similar solution at very small times is likely due to the weak imposition of the chemical-potential boundary condition through Nitsche's method, which effectively regularizes the boundary step over a small numerical layer, in a manner similar to the boundary ramping considered in Bouklas et al. [13], where the boundary chemical potential is imposed gradually over a finite time interval t_{inc}. Beyond this initial discrepancy, both the MPM and FDM results follow the $\sqrt{t}$ scaling up to $t \approx 10\,\tau_d$. Subsequently, the thickness change approaches a constant equilibrium stretch. In the same figure, we also report contours of the stretch in the Y direction, $\lambda(Y,t)$, at eight representative times: $t/\tau_d = 0.0011197$, 0.008589, 0.1281, 0.4531, 1.953, 4.453, 16.06, and 1713. Except for the first contour, which exhibits slight oscillations associated with the abrupt imposition of the boundary chemical potential at $t = 0^+$, the contours remain smooth throughout the simulation, which we attribute to the subdivision-stabilized B-spline discretization. Further validation is provided in Fig. 6c, where the MPM predictions of the chemical potential $\mu/(k_BT)$ as a function of Y are compared against the FDM

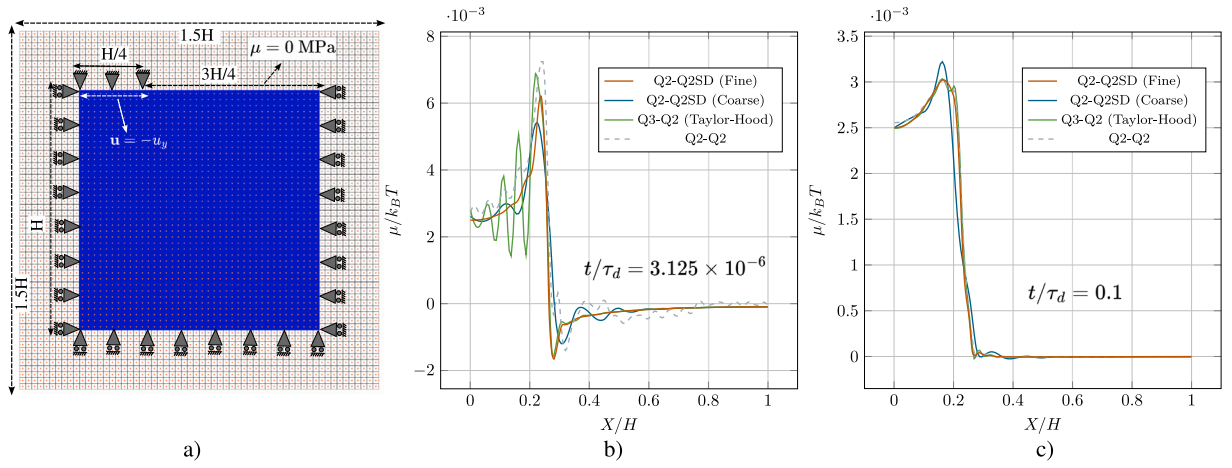

Fig. 7. Flat-punch indentation of hydrogel. **(a)** Problem setup and boundary conditions. **(b)** Top-surface chemical-potential profile, $\mu(X)/(k_BT)$, at the end of the ramp ($t/\tau_d = 3.125 \times 10^{-6}$). The equal-order $Q2$–$Q2$ and Taylor–Hood $Q3$–$Q2$ pairs exhibit spurious oscillations, whereas the fine subdivision-stabilized $Q2$–$Q2$SD pair remains smooth. The coarse subdivision case shows only mild oscillations due to reduced resolution near the boundary and inherent MPM integration error. **(c)** At $t/\tau_d = 0.1$, diffusion regularizes the solution and all discretizations yield smooth, nearly identical chemical-potential profiles.

solution at multiple time instants. The excellent agreement at all times except the earliest one demonstrates both the accuracy and the robustness of the proposed MPM formulation. As noted above, the small oscillations observed at very early times are attributed primarily to the sudden imposition of the boundary chemical potential together with the resulting thin diffusive boundary layer, and should not be interpreted as evidence of a loss of *inf–sup* stability. In the instantaneous-loading limit, the associated diffusion length scales as $\sqrt{D\,\Delta t}$; therefore, sufficiently small time steps require a correspondingly fine spatial discretization to resolve the start-up boundary layer and avoid spurious oscillations. This distinction is examined more directly in the next example, where *inf–sup* unstable discretizations are compared with stable ones. A more detailed discussion of this early-time diffusion-length restriction can be found in Valverde-González et al. [84].

4.2. Flat punch indentation of hydrogel

Next, we consider flat punch indentation of hydrogel as a benchmark to demonstrate the necessity of an *inf–sup* stable discretization for hydrogels under instantaneous loading. As depicted in Fig. 7a, the computational domain is a rectangle of size $1.5H \times 1.5H$, where the hydrogel occupies a square of size $H \times H$ with its bottom–left corner at $(H/4, H/4)$.

To assess the stability of different shape–function pairs and to show why subdivision B-splines are needed, we compare the following $\mathbf{u}$–μ discretizations:

(i) $Q2$–$Q2$ $\left(h_u = h_\mu = 0.05H\right)$: quadratic B-splines for both fields with the same grid (well known to be *inf–sup* unstable).

(ii) $Q3$–$Q2$ $\left(h_u = h_\mu = 0.05H\right)$ (Taylor–Hood): cubic for displacement and quadratic for chemical potential with the highest possible continuity in both fields with same grid. We use $Q3$–$Q2$ rather than $Q2$–$Q1$ to avoid the cell-crossing errors associated with linear ($Q1$) basis functions in MPM. It is important to note, however, that the classical Taylor–Hood pair is *inf–sup* stable in the finite element setting with C^0 inter-element continuity [13], whereas its isogeometric counterpart with maximally smooth C^{q-1} basis functions does not satisfy the *inf–sup* condition [72,74].

(iii) $Q2$–$Q2$SD $\left(h_u = 0.5h_\mu = 0.025H\right)$: subdivision-stabilized quadratic B-splines with a refined displacement grid and a coarser chemical-potential grid (as described in Section 3.4).

(iv) $Q2$–$Q2$SD $\left(h_u = 0.5h_\mu = 0.05H\right)$: a coarser subdivision-stabilized pair used to provide a complementary comparison with (i)–(ii).

The two subdivision-stabilized cases are included because the non-matching element resolutions of the displacement and chemical-potential fields make a single "fair" comparison ambiguous; case (iii) matches the μ resolution of (i)–(ii), while case (iv) matches their $\mathbf{u}$ resolution. In all cases, each active displacement cell inside the gel contains 5×5 material points. Except for μ_0 and λ_0, the material parameters are the same as those listed in Table 1. Here, we assume that the gel is initially swollen in equilibrium with $\mu_0 = 0$. The corresponding pre-stretch, $\lambda_0 = 2.3488$, is obtained directly from Eq. (22). Roller conditions ($\mathbf{u} \cdot \mathbf{N}_n = 0$) and zero–flux ($\mathbf{j}_n \cdot \mathbf{N}_n = 0$) are imposed on the bottom, left, and right boundaries. The characteristic diffusion timescale based on the initial configuration can be obtained as $\tau_d = H^2/D$. On the top boundary, a contiguous segment occupying one quarter of its length is prescribed a compressive displacement $\bar{u}_y = -0.09H$, ramped linearly over $t_{\text{inc}}/\tau_d = 3.125 \times 10^{-6}$. For $t > t_{\text{inc}}$, this displacement is held fixed until $t_{\text{final}}/\tau_d = 2300$ to allow solvent to diffuse and the excess chemical potential (pore pressure) to relax. The remaining

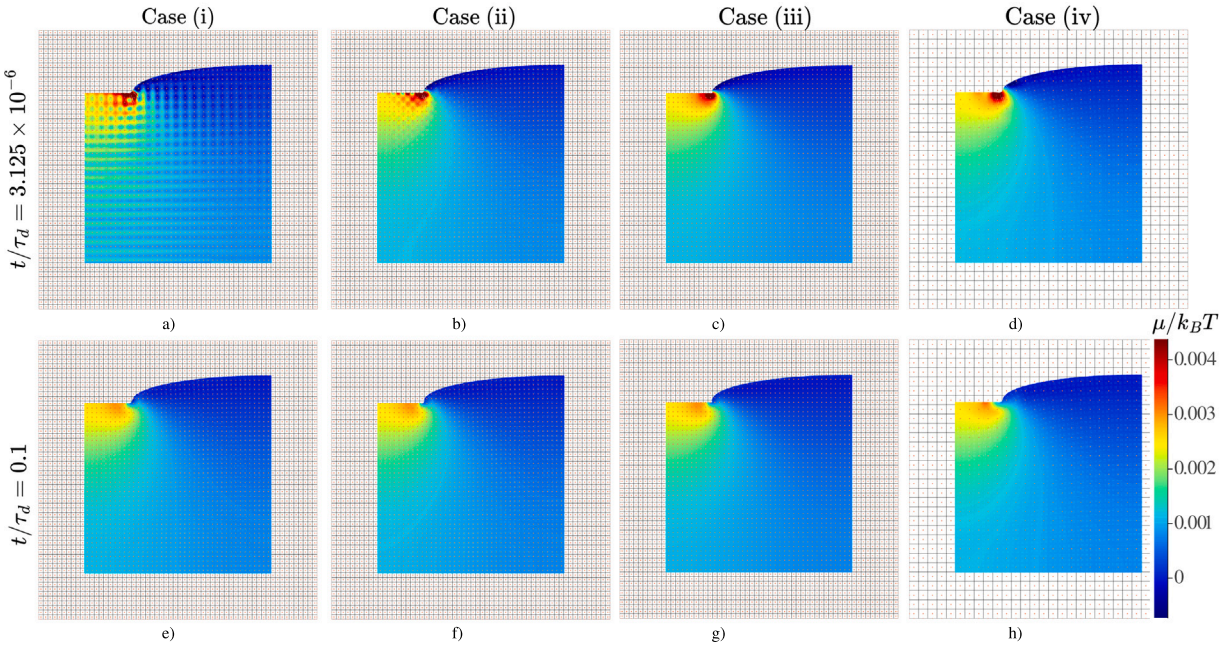

Fig. 8. Flat-punch indentation benchmark: contours of the chemical potential μ/k_BT obtained from the four **u**–μ discretizations. Columns: **(a&e)** equal–order $Q2$–$Q2$, **(b&f)** Taylor–Hood $Q3$–$Q2$, **(c&g)** subdivision–stabilized $Q2$–$Q2$SD (finer), and **(d&h)** subdivision–stabilized $Q2$–$Q2$SD (coarser). Rows: **(a–d)** end of the loading ramp, $t/\tau_d = 3.125 \times 10^{-6}$; **(e–h)** during the early post-ramp diffusion-driven relaxation, $t/\tau_d = 0.1$. At $t = t_{\text{inc}}$ the equal–order $Q2$–$Q2$ and Taylor–Hood pairs **(a&b)** exhibit spurious oscillations in μ/k_BT, whereas the subdivision-stabilized pairs **(c&d)** remain smooth, evidencing *inf–sup* stability. At later times, diffusion regularizes all cases **(e–h)**.

three-quarters of the top boundary are traction–free; to mimic immersion in solvent, their chemical potential is maintained at $\mu = 0$ throughout the simulation. The simulation is started with a fixed time step of $\Delta t = 3.125 \times 10^{-7}\tau_d$ for $t \le t_{\text{inc}}$. Beyond this stage, the time step is adapted based on the nonlinear solver performance, as discussed before.

Fig. 8 shows contours of the chemical potential $\mu/(k_BT)$ at two representative times for the four discretizations.

(i) At the end of the loading ramp, $t = t_{\text{inc}}$ (Fig. 8a–d), the $Q2$–$Q2$ and $Q3$–$Q2$ discretizations exhibit spurious oscillations in μ, whereas the subdivision–stabilized discretizations produce smooth fields. These results are consistent with those reported by Dortdivanlioglu et al. [73] for hydrogels under instantaneous loading and by Ali Madadi and Dortdivanlioglu [72] for hyperelasticity.

(ii) Shortly after loading, at $t/\tau_d = 0.1$ (Fig. 8e–h), all cases appear smooth—the diffusive operator regularizes the chemical–potential field, consistent with the proof in Dortdivanlioglu et al. [73], which shows that diffusion operator adds coercivity to the variational formulation and relaxes the *inf–sup* requirement relative to pure hyperelasticity.

Although the contour plots are shown only up to the reported times, the simulation is continued until $t_{\text{end}}/\tau_d = 2300$, by which point the chemical-potential field has essentially reached equilibrium with $\mu/(k_BT) \approx 0$ throughout the domain. To quantify spurious oscillations in the chemical-potential field, we plot $\mu/(k_BT)$ along the top surface at two representative times, $t = t_{\text{inc}}$ and $t/\tau_d = 0.1$ (Fig. 7b, c). At $t = t_{\text{inc}}$ (Fig. 7b), the fine $Q2$–$Q2$SD discretization produces smooth $\mu/(k_BT)$ profiles, consistent with its *inf–sup* stability, whereas the Taylor–Hood $Q3$–$Q2$ and equal-order $Q2$–$Q2$ pairs exhibit pronounced oscillations. The coarse $Q2$–$Q2$SD case shows only mild oscillations, which we attribute to standard MPM approximation errors and reduced resolution near the boundary. By $t/\tau_d = 0.1$ (Fig. 7c), diffusion has regularized the response, and all discretizations yield smooth chemical-potential profiles. The slight departure from $\mu/(k_BT) = 0$ over the solvent-exposed portion of the top boundary in Fig. 7 is due to the weak imposition of the Dirichlet condition $\mu = 0$ through Nitsche's method; with a deliberately moderate penalty parameter, chosen to avoid over-penalization and ill-conditioning, the condition is enforced consistently but not pointwise.

4.3. Swell-induced buckling of a hydrogel column

In the next example, we examine a two-dimensional hydrogel column immersed within a rectangular computational grid, as depicted in Fig. 9a. The computational domain dimensions are $17.5H \times 10H$, with the hydrogel column measuring $8H \times H$ initially and its bottom–left corner positioned at (H, H). The displacement field is discretized using a fine 350×200 quadratic grid, whereas the chemical potential field employs a coarser 175×100 quadratic grid. Each active computational cell within the hydrogel is

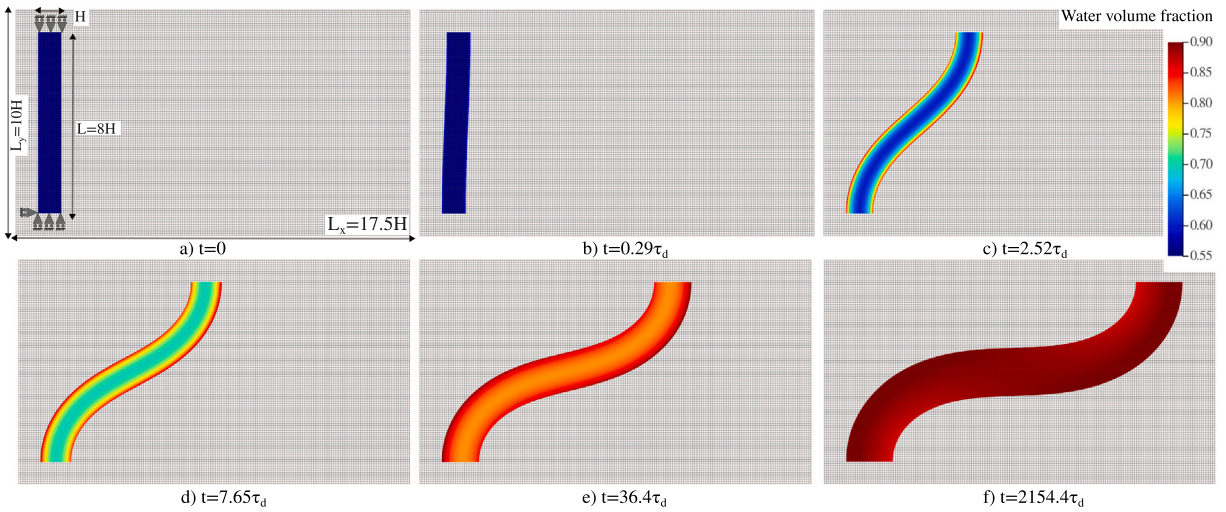

Fig. 9. **(a)** Schematic of the boundary conditions and geometry for the simulation of swell-induced buckling of a hydrogel column. **(b–f)** Contours of solvent volume fraction at selected time steps, illustrating the evolution of swelling-induced instability. The characteristic diffusion timescale based on the initial configuration is $\tau_d = H^2/4D$.

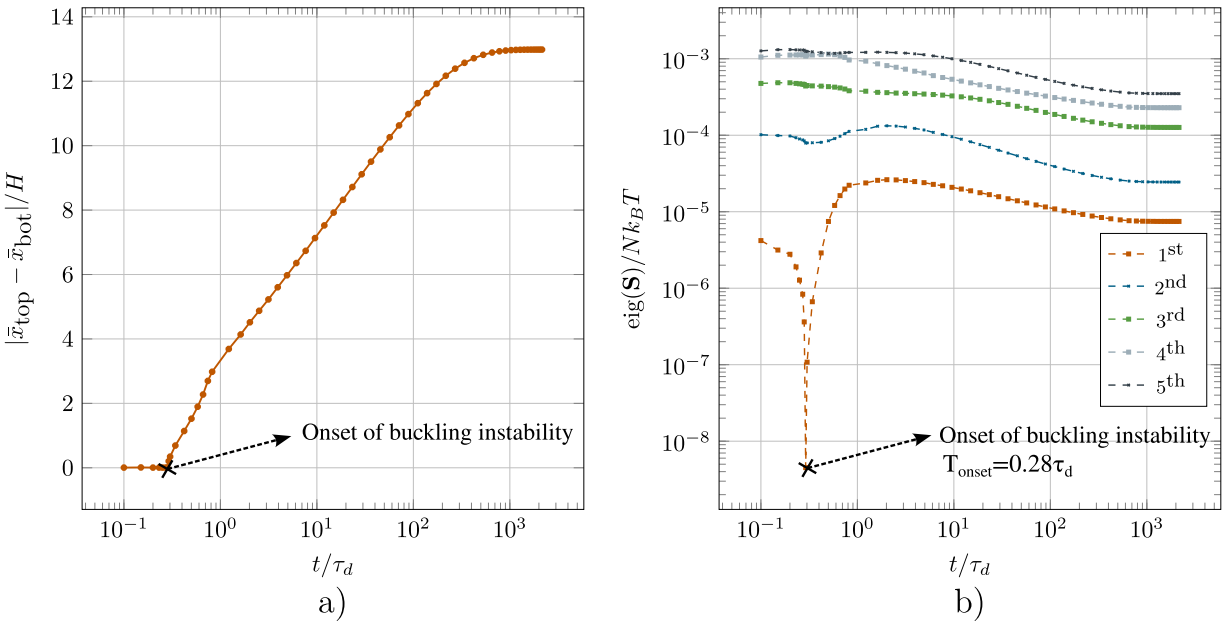

Fig. 10. **(a)** Time history of the separation between the centers of the top and bottom surfaces, highlighting the onset of buckling instability. **(b)** Five smallest eigenvalues of the reduced (Schur-complement) stiffness matrix **S**. A pronounced drop in the smallest eigenvalue marks the onset of instability at $t_{onset} = 0.28\,\tau_d$, while the remaining eigenvalues stay positive.

represented by an 8×8 grid of material points. The material properties employed here are identical to those in Table 1. The characteristic diffusion timescale based on the initial configuration is $\tau_d = H^2/4D$. A boundary condition of $\mu = \mu_0(1 - t/t_{inc})$ is applied incrementally on the left and right surfaces over $t_{inc} = 0.75\,\tau_d$ and then held fixed until the chemical potential becomes uniformly zero throughout the domain. The simulation is terminated at that point ($t_{final} = 2154.4\,\tau_d$). Symmetry boundary conditions ($\mathbf{u} \cdot \mathbf{N}_n = 0$, and zero-flux) are enforced on the top and bottom boundaries by imposing essential boundary conditions of the form $\mathbf{u} \cdot \mathbf{N}_n = 0$. To prevent rigid-body motion, we impose an additional constraint $\mathbf{u} \cdot \mathbf{N}_n = 0$ on a $0.05H$-long segment of the left boundary near the bottom corner. To ensure numerical stability, we utilize an adaptive time-stepping scheme based on monitoring the signature of the stiffness matrix. The simulation begins with a time increment of $\Delta t = 0.1\tau_d$, which is then adaptively adjusted based on the convergence behavior of the Newton–Raphson iterations.

Fig. 9 summarizes the coupled swelling and buckling response of the plane-strain hydrogel column. At the initial state (Fig. 9a), the solvent volume fraction is approximately 0.55. As the boundary chemical potential increases, solvent is absorbed and the

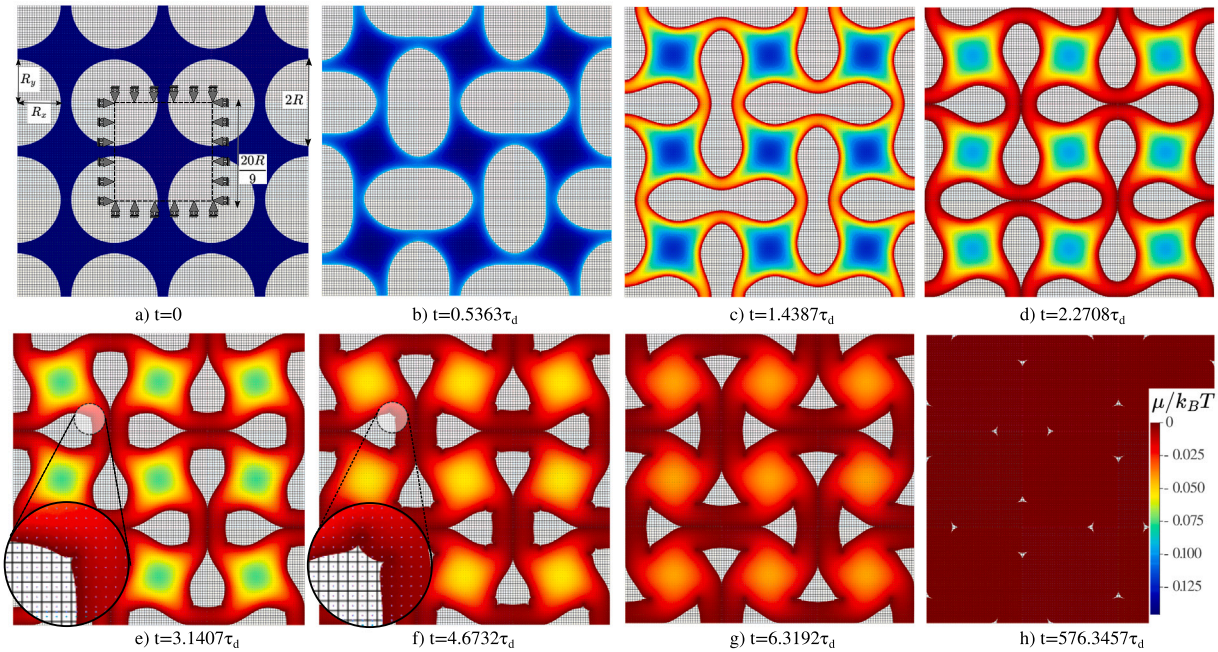

Fig. 11. Hydrogel with a square lattice of cylindrical holes undergoes a symmetry-breaking bifurcation into a periodic array of ellipses with alternating orientations, followed by self-contact and creasing instability. **(a)** Initial undeformed configuration. All four sides of the square domain are constrained using symmetry boundary conditions. **(b–h)** Contours of chemical potential at selected time steps, illustrating bifurcation, self-contact, and surface creasing (e and f). The characteristic diffusion timescale based on the maximum length in the initial configuration is $\tau_d = R^2/(81D)$.

column swells, so that the solvent volume fraction rises, reaching about 0.9 by the final configuration shown in Fig. 9f. Because the column is constrained at both ends, axial extension is suppressed, and compressive stress accumulates in the column. When the swelling-induced compressive stress reaches a critical level (at $t_{\text{onset}} \approx 0.28\,\tau_d$; see Fig. 9b), the column loses stability and buckles. The onset and subsequent evolution of the buckling instability are quantified in Fig. 10. Fig. 10a reports the time history of the separation between the centers of the top and bottom surfaces, exhibiting a clear transition at $t = t_{\text{onset}}$ for the onset of buckling. In parallel, Fig. 10b shows the five smallest eigenvalues of the reduced (Schur-complement) stiffness matrix **S**. The sharp collapse of the smallest eigenvalue toward zero near $t = t_{\text{onset}}$ indicates the loss of stability, whereas the next four eigenvalues remain strictly positive, confirming that only a single mode becomes unstable at the onset. The post-buckling swelling response is illustrated in Fig. 9c–f. Notably, the solvent volume fraction contours remain smooth throughout the simulation, indicating that the subdivision-stabilized extended B-spline discretization robustly resolves the coupled large-deformation and diffusion through the onset of buckling instability and into the post-buckling regime.

4.4. Swell-induced bifurcation of a hydrogel with a square lattice of cylindrical holes

In this final example, we simulate swell-induced bifurcation in a hydrogel containing a periodic square lattice of cylindrical voids. Closely related problems have been investigated experimentally [85,86] and computationally [87,88]. The computational domain, shown in Fig. 11a, measures $20R/9 \times 20R/9$, where R denotes the radius of each cylindrical hole in the domain. For visual clarity, we replicate this cell in a 3×3 array in Fig. 11, so the panel spans $20R/3 \times 20R/3$; only the central cell is actually simulated. Its four edges are constrained in the normal direction to satisfy the reflection–symmetry conditions of the periodic structure. A quadratic background grid with spacings $h_u = R/36$ for the displacement field and $h_\mu = 2h_u$ for the chemical-potential field is employed, while 211,410 material points discretize the solid skeleton. The material parameters are listed in Table 1. The chemical potential on the four quarter-circular cavity boundaries (represented by 354 surface particles) is ramped linearly to zero over $t_{\text{inc}} = 122.4\,\tau_d$ and held fixed thereafter up to $t_{\text{final}} = 576.3\,\tau_d$, where the characteristic diffusion time is defined as $\tau_d = R^2/(81D)$. The simulation is initialized with a time step $\Delta t = 9.455 \times 10^{-2}\,\tau_d$. As in the previous examples, Δt is updated based on Newton–Raphson behavior. In addition, to limit the deformation increment per step, we enforce stage-wise upper bounds on the time step:

$$\Delta t/\tau_d \leq \begin{cases} 7.5643 \times 10^{-2} & 0 < t/\tau_d \leq 7.5643 \\ 1.5129 & 7.5643 < t/\tau_d \leq 26.4750 \\ 7.5643 & 26.4750 < t/\tau_d \leq 60.5144\,. \end{cases} \tag{65}$$

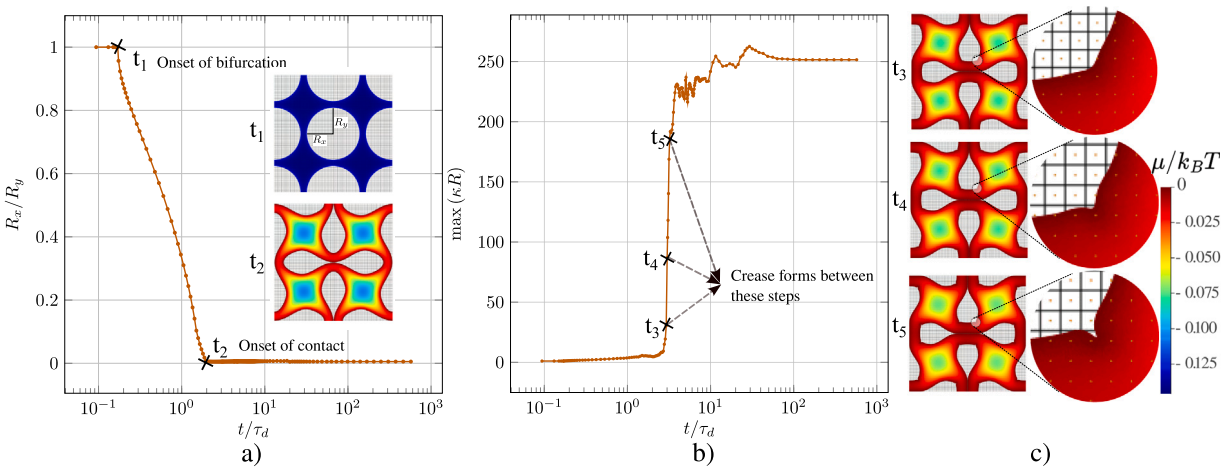

Fig. 12. **(a)** Time evolution of the ratio between the two principal pore radii, highlighting the symmetry-breaking bifurcation and self-contact due to swelling. Inset(top): deformed pore geometry with overlaid chemical-potential contours immediately after onset of bifurcation; Inset(bottom): deformation and chemical potential contours at the onset of self-contact. **(b)** Time evolution of the normalized peak surface curvature, marking the onset of crease formation. **(c)** Before–after views of crease formation, showing the evolution of the crease from an edged surface at t_3, through an intermediate cup-shaped stage at t_4 with an emerging localized indentation, into a localized deformation at t_5 over a very short time.

Fig. 11 shows the complete deformation sequence along with contours of the chemical potential field. Initially, diffusion-driven swelling causes each cylindrical pore to shrink nearly uniformly in all directions. At approximately $t \approx 0.171\,\tau_d$, the system reaches a critical chemical potential of $\mu/(k_B T) = -0.13$, which triggers a *symmetry-breaking bifurcation*. Consequently, the initially circular pores elongate into ellipses, with their major axes alternating between horizontal and vertical orientations (Fig. 11b). This transition is quantified in Fig. 12a, where the ratio of the principal pore radii sharply deviates from unity, clearly indicating the onset of bifurcation.

Continued solvent uptake pushes the elliptical tips into *self-contact* at approximately $t \approx 2\,\tau_d$ (Fig. 12a, bottom inset). Subsequently, the area of contact increases and each pore splits into two, creating flattened ends with sharp corners. The deformation near the corners is highly localized, leading to surface creases by self-folding, as shown in Fig. 11e. We quantify this creasing behavior by plotting the maximum surface curvature over time in Fig. 12b. The maximum curvature increases sharply at around $t \approx 3\,\tau_d$, marking the initiation of *creasing* characterized by sharp, self-contacting folds of the pore surface. Fig. 12c shows three selected time steps during crease formation, including two consecutive time steps, $t_3 = 2.95\tau_d$ and $t_4 = 3.025\tau_d$, followed by a later time, $t_5 = 3.248\tau_d$. The insets highlight the surface region where the crease nucleates, evolves through an intermediate cup-shaped stage, and then further localizes, with the maximum change in surface curvature occurring between t_3 and t_4.

After the first crease nucleates at each corner, continued swelling promotes additional creasing; by $t = 4.6732\,\tau_d$, a second crease is clearly visible (Fig. 11f). Further swelling leads to sharp folds of the pore surface as the pore shrinks (Fig. 11g–h). The MPM simulation proceeds until the chemical potential becomes essentially uniform, at which point the swollen gel occupies nearly the entire computational domain (Fig. 11h). Throughout this highly nonlinear sequence, encompassing symmetry breaking, self-contact, and surface creasing, the chemical-potential field remains smooth and free of spurious oscillations, underscoring the robustness of the subdivision-stabilized extended B-spline discretization. Overall, this example demonstrates that the MPM framework can reliably resolve swelling-induced instabilities in a hydrogel while maintaining accurate tracking of the evolving fields of chemical potential and large deformation. This example also highlights the particular advantage of MPM for problems involving extreme deformation, self-contact, and highly localized creasing, which are difficult to resolve robustly with standard mesh-conforming Lagrangian methods because of severe mesh distortion.

We note that self-contact in the present simulation is handled implicitly rather than through a dedicated contact algorithm. As opposing pore surfaces approach one another, material points on the two sides interact through the same background grid nodes and thus share the same interpolated nodal field. As a result, further relative motion across the interface is effectively suppressed, leading to an approximate tied-contact response once contact is established. Because this interaction is activated by the common support of the background-grid basis functions, the effective contact distance is mesh dependent: coarser grids produce contact at a larger contact gap, whereas refinement reduces the contact gap. This behavior is illustrated in Fig. 13, which shows the single simulated unit cell (rather than the 3×3 replicated visualization used in Fig. 11h) at the final time for three background-grid resolutions. Relative to the reference discretization with $h_u = R/36$, the numbers of volume and surface material points are scaled consistently for the coarser and finer grids so that the material-point density relative to the background grid is maintained. Enlarged views of the contact region also show the volume and surface material points together with the background grid.

This treatment is sufficient for the present study, which focuses on pore collapse and surface creasing under continued swelling. Nevertheless, because no explicit contact law is enforced, the formulation should not be regarded as a general self-contact framework. In particular, standard MPM may exhibit artificial sticking when sliding or separation after contact becomes important. More

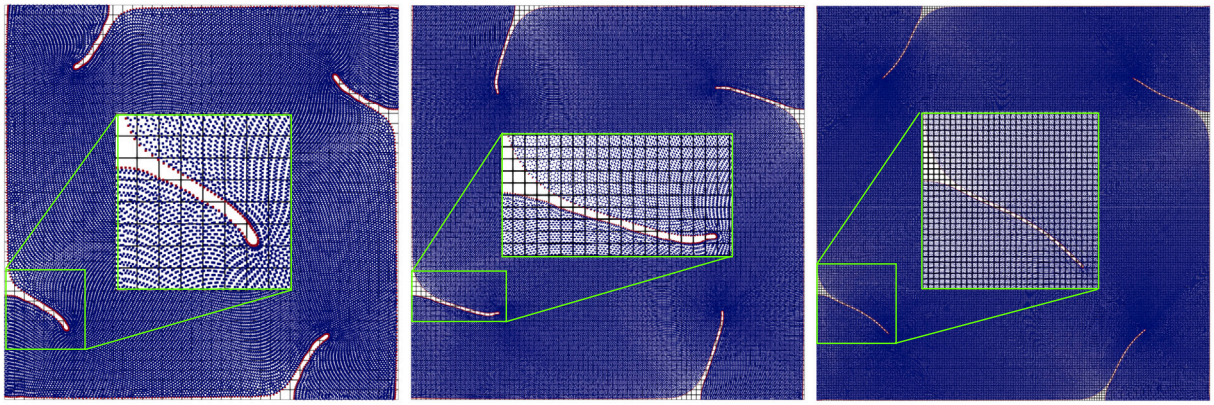

a) $h_{\mathbf{u}} = R/18$ b) $h_{\mathbf{u}} = R/36$ c) $h_{\mathbf{u}} = R/72$

Fig. 13. Final configuration of the single simulated unit cell for three background-grid resolutions. The volume and surface material-point densities are scaled consistently with the grid. Insets show the contact region, background grid (black), volume material points (blue), and surface material points (red). The contact gap decreases with mesh refinement because contact is mediated through the common support of the background-grid basis functions.

advanced contact treatments, such as penalty-based, level-set-based, or Nitsche-type methods [89–91], could be introduced if accurate post-contact behaviors were required.

5. Conclusion

In this work, we generalize the *extended B-spline* mixed MPM [24] to a fully coupled diffusion–hyperelastic formulation for hydrogels. The formulation combines (i) subdivision-stabilized B-spline spaces to obtain an *inf–sup* stable $\mathbf{u}$–μ discretization, (ii) extended B-splines to cure cut-cell ill-conditioning, and (iii) a symmetric Nitsche scheme to impose Dirichlet boundary conditions on immersed boundaries. Together, these ingredients control cell-crossing errors, suppress volumetric locking as $\Delta t \to 0$, and yield a symmetric, well-conditioned tangent suitable for stability analysis. Stability is assessed either via the smallest eigenvalues of the reduced (Schur-complement) stiffness or, equivalently, by tracking the inertia (signature) of the full tangent matrix. We verified the framework and demonstrated its robustness under very large deformations using challenging benchmark problems, including buckling of a swollen hydrogel column as well as bifurcation and surface creasing in a porous hydrogel with cylindrical pores. The simulations exhibit smooth chemical potential fields and reliable results, highlighting the effectiveness of the mixed isogeometric MPM. Future work will extend the framework to additional multiphysics soft-matter systems (e.g., dielectric elastomers and polyelectrolyte gels), incorporate interfaces and frictional contact using Nitsche's method, and investigate adaptive cell subdivision or octree-based quadrature [92–94] to improve MPM integration accuracy under extreme swelling.

CRediT authorship contribution statement

Ashkan Ali Madadi: Writing – original draft, Visualization, Validation, Software, Methodology, Investigation, Formal analysis, Data curation, Conceptualization. **Thomas J.R. Hughes:** Writing – review & editing, Supervision, Methodology, Conceptualization, Funding acquisition. **Rui Huang:** Writing – review & editing, Supervision, Methodology, Conceptualization,Funding acquisition.

Declaration of competing interest

The authors declare that they have no known competing financial interests or personal relationships that could have appeared to influence the work reported in this paper.

Acknowledgments

The authors gratefully acknowledge funding from the U.S. National Science Foundation (NSF) under Award No. CMMI-2549543.

Data availability

Data will be made available on request.

References

[1] N. Yan, R. Sujanani, J. Kamcev, E.-S. Jang, K. Kobayashi, D.R. Paul, B.D. Freeman, Salt and ion transport in a series of crosslinked AMPS/PEGDA hydrogel membranes, J. Membr. Sci. 653 (2022) 120549, http://dx.doi.org/10.1016/j.memsci.2022.120549.

[2] D. Nikolaeva, C. Langner, A. Ghanem, M.A. Rehim, B. Voit, J. Meier-Haack, Hydrogel surface modification of reverse osmosis membranes, J. Membr. Sci. 476 (2015) 264–276, http://dx.doi.org/10.1016/j.memsci.2014.11.051.

[3] W. Fu, J. Chen, C. Li, L. Jiang, M. Qiu, X. Li, Y. Wang, L. Cui, Enhanced flux and fouling resistance forward osmosis membrane based on a hydrogel/MOF hybrid selective layer, J. Colloid Interface Sci. 585 (2021) 158–166, http://dx.doi.org/10.1016/j.jcis.2020.11.092.

[4] A. Ullah, D.Y. Kim, S.I. Lim, H.-R. Lim, Hydrogel-based biointerfaces: Recent advances, challenges, and future directions in human–machine integration, Gels 11 (4) (2025) http://dx.doi.org/10.3390/gels11040232.

[5] S. Wang, Q. Zhao, J. Li, X. Du, Morphing-to-adhesion polysaccharide hydrogel for adaptive biointerfaces, ACS Appl. Mater. Interfaces 14 (37) (2022) 42420–42429, http://dx.doi.org/10.1021/acsami.2c10117.

[6] K. Zhang, X. Chen, Y. Xue, J. Lin, X. Liang, J. Zhang, J. Zhang, G. Chen, C. Cai, J. Liu, Tough hydrogel bioadhesives for sutureless wound sealing, hemostasis and biointerfaces, Adv. Funct. Mater. 32 (15) (2022) 2111465, http://dx.doi.org/10.1002/adfm.202111465.

[7] Z. Jiang, P. Song, Strong and fast hydrogel actuators, Science 376 (6590) (2022) 245, http://dx.doi.org/10.1126/science.abo4603.

[8] D. Jiao, Q.L. Zhu, C.Y. Li, Q. Zheng, Z.L. Wu, Programmable morphing hydrogels for soft actuators and robots: From structure designs to active functions, Acc. Chem. Res. 55 (11) (2022) 1533–1545, http://dx.doi.org/10.1021/acs.accounts.2c00046.

[9] A. Zolfagharian, A.Z. Kouzani, S.Y. Khoo, I. Gibson, A. Kaynak, 3D printed hydrogel soft actuators, in: 2016 IEEE Region 10 Conference, TENCON, 2016, pp. 2272–2277, http://dx.doi.org/10.1109/TENCON.2016.7848433.

[10] F. Weiss, S. Cai, Y. Hu, M.K. Kang, R. Huang, Z. Suo, Creases and wrinkles on the surface of a swollen gel, J. Appl. Phys. 114 (7) (2013) 073507, http://dx.doi.org/10.1063/1.4818943.

[11] M.K. Kang, R. Huang, Swelling-induced instability of substrate-attached hydrogel lines, Int. J. Appl. Mech. 03 (02) (2011) 219–233, http://dx.doi.org/10.1142/S1758825111000956.

[12] M.K. Kang, R. Huang, Swell-induced surface instability of confined hydrogel layers on substrates, J. Mech. Phys. Solids 58 (10) (2010) 1582–1598, http://dx.doi.org/10.1016/j.jmps.2010.07.008.

[13] N. Bouklas, C.M. Landis, R. Huang, A nonlinear, transient finite element method for coupled solvent diffusion and large deformation of hydrogels, J. Mech. Phys. Solids 79 (2015) 21–43, http://dx.doi.org/10.1016/j.jmps.2015.03.004.

[14] L. Böger, A. Nateghi, C. Miehe, A minimization principle for deformation-diffusion processes in polymeric hydrogels: Constitutive modeling and FE implementation, Int. J. Solids Struct. 121 (2017) 257–274, http://dx.doi.org/10.1016/j.ijsolstr.2017.05.034.

[15] B. Dortdivanlioglu, C. Linder, Diffusion-driven swelling-induced instabilities of hydrogels, J. Mech. Phys. Solids 125 (2019) 38–52, http://dx.doi.org/10.1016/j.jmps.2018.12.010.

[16] S. Rajendran, A technique to develop mesh-distortion immune finite elements, Comput. Methods Appl. Mech. Engrg. 199 (17) (2010) 1044–1063, http://dx.doi.org/10.1016/j.cma.2009.11.017.

[17] İ. Temizer, P. Wriggers, T. Hughes, Contact treatment in isogeometric analysis with NURBS, Comput. Methods Appl. Mech. Engrg. 200 (9) (2011) 1100–1112, http://dx.doi.org/10.1016/j.cma.2010.11.020.

[18] D. Sulsky, Z. Chen, H. Schreyer, A particle method for history-dependent materials, Comput. Methods Appl. Mech. Engrg. 118 (1) (1994) 179–196, http://dx.doi.org/10.1016/0045-7825(94)90112-0.

[19] R. Hill, On uniqueness and stability in the theory of finite elastic strain, J. Mech. Phys. Solids 5 (4) (1957) 229–241, http://dx.doi.org/10.1016/0022-5096(57)90016-9.

[20] M.A. Biot, Mechanics of Incremental Deformations: Theory of Elasticity and Viscoelasticity of Initially Stressed Solids and Fluids, Including Thermodynamic Foundations and Applications to Finite Strain, Routledge, 1965.

[21] F. Auricchio, L. Beirão da Veiga, C. Lovadina, A. Reali, A stability study of some mixed finite elements for large deformation elasticity problems, Comput. Methods Appl. Mech. Engrg. 194 (9) (2005) 1075–1092, http://dx.doi.org/10.1016/j.cma.2004.06.014.

[22] F. Auricchio, L. Beirão da Veiga, C. Lovadina, A. Reali, R.L. Taylor, P. Wriggers, Approximation of incompressible large deformation elastic problems: Some unresolved issues, Comput. Mech. 52 (5) (2013) 1153–1167, http://dx.doi.org/10.1007/s00466-013-0869-0.

[23] J. Schröder, N. Viebahn, P. Wriggers, F. Auricchio, K. Steeger, On the stability analysis of hyperelastic boundary value problems using three- and two-field mixed finite element formulations, Comput. Mech. 60 (3) (2017) 479–492, http://dx.doi.org/10.1007/s00466-017-1415-2.

[24] A. Ali Madadi, B. Dortdivanlioglu, Extended mixed B-spline material point method with Nitsche's method for quasi-compressible soft materials, Internat. J. Numer. Methods Engrg. 126 (22) (2025) e70185, http://dx.doi.org/10.1002/nme.70185.

[25] A. de Vaucorbeil, V.P. Nguyen, S. Sinaie, J.Y. Wu, Chapter two - material point method after 25 years: Theory, implementation, and applications, Adv. Appl. Mech. 53 (2020) 185–398, http://dx.doi.org/10.1016/bs.aams.2019.11.001.

[26] E.M.K. S. G. Bardenhagen, The generalized interpolation material point method, Comput. Model. Eng. Sci. 5 (6) (2004) 477–496, http://dx.doi.org/10.3970/cmes.2004.005.477.

[27] A. Sadeghirad, R. Brannon, J. Guilkey, Second-order convected particle domain interpolation (CPDI2) with enrichment for weak discontinuities at material interfaces, Internat. J. Numer. Methods Engrg. 95 (11) (2013) 928–952, http://dx.doi.org/10.1002/nme.4526.

[28] A. Sadeghirad, R.M. Brannon, J. Burghardt, A convected particle domain interpolation technique to extend applicability of the material point method for problems involving massive deformations, Internat. J. Numer. Methods Engrg. 86 (12) (2011) 1435–1456, http://dx.doi.org/10.1002/nme.3110.

[29] R. Noh, A.A. Madadi, B. Dortdivanlioglu, Modeling surface tension in fluid membranes and soft materials using surface-enriched convected particle domain interpolation (CPDI), Comput. Mech. (2026) http://dx.doi.org/10.1007/s00466-026-02804-8.

[30] D.Z. Zhang, X. Ma, P.T. Giguere, Material point method enhanced by modified gradient of shape function, J. Comput. Phys. 230 (16) (2011) 6379–6398, http://dx.doi.org/10.1016/j.jcp.2011.04.032.

[31] P.L. Barclay, J. Waters, D.Z. Zhang, Large deformation and brittle failure calculated using the dual-domain material point method, Comput. Part. Mech. (2023) http://dx.doi.org/10.1007/s40571-023-00615-9.

[32] X. Ma, D.Z. Zhang, P.T. Giguere, C. Liu, Axisymmetric computation of Taylor cylinder impacts of ductile and brittle materials using original and dual domain material point methods, Int. J. Impact Eng. 54 (2013) 96–104, http://dx.doi.org/10.1016/j.ijimpeng.2012.11.001.

[33] T.R. Dhakal, D.Z. Zhang, Material point methods applied to one-dimensional shock waves and dual domain material point method with sub-points, J. Comput. Phys. 325 (2016) 301–313, http://dx.doi.org/10.1016/j.jcp.2016.08.033.

[34] M. Steffen, R.M. Kirby, M. Berzins, Analysis and reduction of quadrature errors in the material point method (MPM), Internat. J. Numer. Methods Engrg. 76 (6) (2008) 922–948, http://dx.doi.org/10.1002/nme.2360.

[35] A. de Vaucorbeil, V.P. Nguyen, C.R. Hutchinson, A Total-Lagrangian Material Point Method for solid mechanics problems involving large deformations, Comput. Methods Appl. Mech. Engrg. 360 (2020) 112783, http://dx.doi.org/10.1016/j.cma.2019.112783.

[36] Y. Gan, Z. Sun, Z. Chen, X. Zhang, Y. Liu, Enhancement of the material point method using B-spline basis functions, Internat. J. Numer. Methods Engrg. 113 (3) (2018) 411–431, http://dx.doi.org/10.1002/nme.5620.

[37] G. Moutsanidis, C.C. Long, Y. Bazilevs, IGA-MPM: The Isogeometric Material Point Method, Comput. Methods Appl. Mech. Engrg. 372 (2020) 113346, http://dx.doi.org/10.1016/j.cma.2020.113346.

[38] R. Tielen, E. Wobbes, M. Möller, L. Beuth, A high order material point method, Procedia Eng. 175 (2017) 265–272, http://dx.doi.org/10.1016/j.proeng.2017.01.022, Proceedings of the 1st International Conference on the Material Point Method (MPM 2017).

[39] Y. Yamaguchi, S. Moriguchi, K. Terada, Extended B-spline-based implicit material point method, Internat. J. Numer. Methods Engrg. 122 (7) (2021) 1746–1769, http://dx.doi.org/10.1002/nme.6598.

[40] Z. Sun, Y. Gan, J. Tao, Z. Huang, X. Zhou, An improved quadrature scheme in B-spline material point method for large-deformation problem analysis, Eng. Anal. Bound. Elem. 138 (2022) 301–318, http://dx.doi.org/10.1016/j.enganabound.2022.03.004.

[41] Z. Sun, Y. Gan, Z. Huang, X. Zhou, A local grid refinement scheme for B-spline material point method, Internat. J. Numer. Methods Engrg. 121 (11) (2020) 2398–2417, http://dx.doi.org/10.1002/nme.6312.

[42] M. Neuner, A. Dummer, S. Abrari Vajari, P. Gamnitzer, H. Gimperlein, C. Linder, G. Hofstetter, A B-spline based gradient-enhanced micropolar implicit material point method for large localized inelastic deformations, Comput. Methods Appl. Mech. Engrg. 431 (2024) 117291, http://dx.doi.org/10.1016/j.cma.2024.117291.

[43] A. Alsardi, A. Yerro, C.C. Long, Enhanced mpm framework with multipatch isogeometric analysis for geotechnical applications, 2025, http://dx.doi.org/10.2139/ssrn.5358326, SSRN.

[44] D. Thomas, M. Scott, J. Evans, K. Tew, E. Evans, Bézier projection: A unified approach for local projection and quadrature-free refinement and coarsening of NURBS and T-splines with particular application to isogeometric design and analysis, Comput. Methods Appl. Mech. Engrg. 284 (2015) 55–105, http://dx.doi.org/10.1016/j.cma.2014.07.014, Isogeometric Analysis Special Issue.

[45] T. Hughes, J. Cottrell, Y. Bazilevs, Isogeometric analysis: CAD, finite elements, NURBS, exact geometry and mesh refinement, Comput. Methods Appl. Mech. Engrg. 194 (39) (2005) 4135–4195, http://dx.doi.org/10.1016/j.cma.2004.10.008.

[46] Y.T. Elbadry, P. Antolín, O. Weeger, Immersed isogeometric analysis with boundary conformal quadrature for finite deformation elasticity, Arch. Appl. Mech. 95 (9) (2025) 219, http://dx.doi.org/10.1007/s00419-025-02924-2.

[47] V. Singer, T. Teschemacher, A. Larese, R. Wüchner, K.-U. Bletzinger, Lagrange multiplier imposition of non-conforming essential boundary conditions in implicit material point method, Comput. Mech. 73 (6) (2024) 1311–1333, http://dx.doi.org/10.1007/s00466-023-02412-w.

[48] P. Hansbo, C. Lovadina, I. Perugia, G. Sangalli, A Lagrange multiplier method for the finite element solution of elliptic interface problems using non-matching meshes, Numer. Math. 100 (1) (2005) 91–115, http://dx.doi.org/10.1007/s00211-005-0587-4.

[49] I. Babuška, The finite element method with Lagrangian multipliers, Numer. Math. 20 (3) (1973) 179–192, http://dx.doi.org/10.1007/BF01436561.

[50] Y. Lu, T. Belytschko, L. Gu, A new implementation of the element free Galerkin method, Comput. Methods Appl. Mech. Engrg. 113 (3) (1994) 397–414, http://dx.doi.org/10.1016/0045-7825(94)90056-6.

[51] T. Belytschko, Y. Krongauz, D. Organ, M. Fleming, P. Krysl, Meshless methods: An overview and recent developments, Comput. Methods Appl. Mech. Engrg. 139 (1) (1996) 3–47, http://dx.doi.org/10.1016/S0045-7825(96)01078-X.

[52] T. Zhu, S.N. Atluri, A modified collocation method and a penalty formulation for enforcing the essential boundary conditions in the element free Galerkin method, Comput. Mech. 21 (3) (1998) 211–222, http://dx.doi.org/10.1007/s004660050296.

[53] B. Chandra, V. Singer, T. Teschemacher, R. Wüchner, A. Larese, Nonconforming Dirichlet boundary conditions in implicit material point method by means of penalty augmentation, Acta Geotech. 16 (8) (2021) 2315–2335, http://dx.doi.org/10.1007/s11440-020-01123-3.

[54] S. Fernández-Méndez, A. Huerta, Imposing essential boundary conditions in mesh-free methods, Comput. Methods Appl. Mech. Engrg. 193 (12–14) (2004) 1257–1275, http://dx.doi.org/10.1016/j.cma.2003.12.019.

[55] C. Annavarapu, M. Hautefeuille, J.E. Dolbow, A robust Nitsche's formulation for interface problems, Comput. Methods Appl. Mech. Engrg. 225–228 (2012) 44–54, http://dx.doi.org/10.1016/j.cma.2012.03.008.

[56] C. Annavarapu, M. Hautefeuille, J.E. Dolbow, A Nitsche stabilized finite element method for frictional sliding on embedded interfaces. Part I: Single interface, Comput. Methods Appl. Mech. Engrg. 268 (2014) 417–436, http://dx.doi.org/10.1016/j.cma.2013.09.002.

[57] A. Embar, J. Dolbow, I. Harari, Imposing Dirichlet boundary conditions with Nitsche's method and spline-based finite elements, Internat. J. Numer. Methods Engrg. 83 (7) (2010) 877–898, http://dx.doi.org/10.1002/nme.2863.

[58] J. Nitsche, Über ein Variationsprinzip zur Lösung von Dirichlet-Problemen bei Verwendung von Teilräumen, die keinen Randbedingungen unterworfen sind, in: Abhandlungen aus dem mathematischen Seminar der Universität Hamburg, vol. 36, Springer, 1971, pp. 9–15.

[59] K. Lu, C.E. Augarde, W.M. Coombs, Z. Hu, Weak impositions of Dirichlet boundary conditions in solid mechanics: A critique of current approaches and extension to partially prescribed boundaries, Comput. Methods Appl. Mech. Engrg. 348 (2019) 632–659, http://dx.doi.org/10.1016/j.cma.2019.01.035.

[60] E. Burman, Ghost penalty, Comptes Rendus. Math. 348 (21–22) (2010) 1217–1220, http://dx.doi.org/10.1016/j.crma.2010.10.006.

[61] E. Burman, P. Hansbo, Fictitious domain finite element methods using cut elements: II. A stabilized Nitsche method, Appl. Numer. Math. 62 (4) (2012) 328–341, http://dx.doi.org/10.1016/j.apnum.2011.01.008, Third Chilean Workshop on Numerical Analysis of Partial Differential Equations (WONAPDE 2010).

[62] W.M. Coombs, Ghost stabilisation of the material point method for stable quasi-static and dynamic analysis of large deformation problems, Internat. J. Numer. Methods Engrg. 124 (21) (2023) 4841–4875, http://dx.doi.org/10.1002/nme.7332.

[63] K. Höllig, U. Reif, J. Wipper, Weighted extended B-spline approximation of Dirichlet problems, SIAM J. Numer. Anal. 39 (2) (2001) 442–462, http://dx.doi.org/10.1137/S0036142900373208.

[64] O. Davydov, J. Prasiswa, U. Reif, Two-stage approximation methods with extended B-splines, Math. Comp. 83 (286) (2013) 809–833, http://dx.doi.org/10.1090/S0025-5718-2013-02734-2.

[65] T. Rüberg, F. Cirak, Subdivision-stabilised immersed b-spline finite elements for moving boundary flows, Comput. Methods Appl. Mech. Engrg. 209–212 (2012) 266–283, http://dx.doi.org/10.1016/j.cma.2011.10.007.

[66] B. Marussig, J. Zechner, G. Beer, T.-P. Fries, Stable isogeometric analysis of trimmed geometries, Comput. Methods Appl. Mech. Engrg. 316 (2017) 497–521, http://dx.doi.org/10.1016/j.cma.2016.07.040, Special Issue on Isogeometric Analysis: Progress and Challenges.

[67] B. Marussig, T.J.R. Hughes, A review of trimming in isogeometric analysis: Challenges, data exchange and simulation aspects, Arch. Comput. Methods Eng. 25 (4) (2018) 1059–1127, http://dx.doi.org/10.1007/s11831-017-9220-9.

[68] M.J. Marsden, An identity for spline functions with applications to variation-diminishing spline approximation, J. Approx. Theory 3 (1) (1970) 7–49, http://dx.doi.org/10.1016/0021-9045(70)90058-4.

[69] K. Hollig, Finite element methods with B-splines, in: Frontiers in Applied Mathematics, Society for Industrial and Applied Mathematics, SIAM, 3600 Market Street, Floor 6, Philadelphia, PA 19104, 2003.

[70] F. Brezzi, On the existence, uniqueness and approximation of saddle-point problems arising from Lagrangian multipliers, Publ. Math. Inform. Rennes (1974) 1–26.

[71] C. Miehe, S. Mauthe, H. Ulmer, Formulation and numerical exploitation of mixed variational principles for coupled problems of Cahn–Hilliard-type and standard diffusion in elastic solids, Internat. J. Numer. Methods Engrg. 99 (10) (2014) 737–762, http://dx.doi.org/10.1002/nme.4700.

[72] A. Ali Madadi, B. Dortdivanlioglu, A subdivision-stabilized B-spline mixed material point method, Comput. Methods Appl. Mech. Engrg. 418 (2024) 116567, http://dx.doi.org/10.1016/j.cma.2023.116567.

[73] B. Dortdivanlioglu, A. Krischok, L. Beirão da Veiga, C. Linder, Mixed isogeometric analysis of strongly coupled diffusion in porous materials, Internat. J. Numer. Methods Engrg. 114 (1) (2018) 28–46, http://dx.doi.org/10.1002/nme.5731.
[74] C. Kadapa, W. Dettmer, D. Perić, Subdivision based mixed methods for isogeometric analysis of linear and nonlinear nearly incompressible materials, Comput. Methods Appl. Mech. Engrg. 305 (2016) 241–270, http://dx.doi.org/10.1016/j.cma.2016.03.013.
[75] A. Bressan, G. Sangalli, Isogeometric discretizations of the Stokes problem: Stability analysis by the macroelement technique, IMA J. Numer. Anal. 33 (2) (2013) 629–651, http://dx.doi.org/10.1093/imanum/drr056.
[76] A. Bressan, B. Jüttler, Inf–sup stability of isogeometric Taylor–Hood and Sub-Grid methods for the Stokes problem with hierarchical splines, IMA J. Numer. Anal. 38 (2) (2017) 955–975, http://dx.doi.org/10.1093/imanum/drx031.
[77] P. Antolin, A. Bressan, A. Buffa, G. Sangalli, An isogeometric method for linear nearly-incompressible elasticity with local stress projection, Comput. Methods Appl. Mech. Engrg. 316 (2017) 694–719, http://dx.doi.org/10.1016/j.cma.2016.09.033, Special Issue on Isogeometric Analysis: Progress and Challenges.
[78] T. Rüberg, F. Cirak, A fixed-grid b-spline finite element technique for fluid–structure interaction, Internat. J. Numer. Methods Fluids 74 (9) (2014) 623–660, http://dx.doi.org/10.1002/fld.3864.
[79] W. Hong, X. Zhao, J. Zhou, Z. Suo, A theory of coupled diffusion and large deformation in polymeric gels, J. Mech. Phys. Solids 56 (5) (2008) 1779–1793, http://dx.doi.org/10.1016/j.jmps.2007.11.010.
[80] S.A. Chester, L. Anand, A coupled theory of fluid permeation and large deformations for elastomeric materials, J. Mech. Phys. Solids 58 (11) (2010) 1879–1906, http://dx.doi.org/10.1016/j.jmps.2010.07.020.
[81] N. Bouklas, R. Huang, Swelling kinetics of polymer gels: Comparison of linear and nonlinear theories, Soft Matter 8 (2012) 8194–8203, http://dx.doi.org/10.1039/C2SM25467K.
[82] C. de Boor, Package for calculating with B-splines, SIAM J. Numer. Anal. 14 (1977) 441–472, http://dx.doi.org/10.1137/0714026.
[83] J. Sylvester, XIX. A demonstration of the theorem that every homogeneous quadratic polynomial is reducible by real orthogonal substitutions to the form of a sum of positive and negative squares, Lond. Edinb. Dublin Philos. Mag. J. Sci. 4 (23) (1852) 138–142, http://dx.doi.org/10.1080/14786445208647087.
[84] A. Valverde-González, J. Reinoso, M. Paggi, B. Dortdivanlioglu, Coupled field modeling of thermoresponsive hydrogels with upper/lower critical solution temperature, Extrem. Mech. Lett. 72 (2024) 102222, http://dx.doi.org/10.1016/j.eml.2024.102222.
[85] B. Cao, G. Wu, Y. Xia, S. Yang, Buckling into single-handed chiral structures from pH-sensitive hydrogel membranes, Extrem. Mech. Lett. 7 (2016) 49–54, http://dx.doi.org/10.1016/j.eml.2015.12.011, Mechanics in Extreme Manufacturing.
[86] G. Wu, Y. Xia, S. Yang, Buckling, symmetry breaking, and cavitation in periodically micro-structured hydrogel membranes, Soft Matter 10 (2014) 1392–1399, http://dx.doi.org/10.1039/C3SM51640G.
[87] W. Hong, Z. Liu, Z. Suo, Inhomogeneous swelling of a gel in equilibrium with a solvent and mechanical load, Int. J. Solids Struct. 46 (17) (2009) 3282–3289, http://dx.doi.org/10.1016/j.ijsolstr.2009.04.022.
[88] Z. Ding, Z. Liu, J. Hu, S. Swaddiwudhipong, Z. Yang, Inhomogeneous large deformation study of temperature-sensitive hydrogel, Int. J. Solids Struct. 50 (16) (2013) 2610–2619, http://dx.doi.org/10.1016/j.ijsolstr.2013.04.011.
[89] K. Zhang, S.-L. Shen, H. Wu, A. Zhou, Nitsche-based material point method for large deformation frictional contact problems, Comput. Part. Mech. 12 (2) (2025) 947–970, http://dx.doi.org/10.1007/s40571-024-00846-4.
[90] E.G. Kakouris, M.N. Chatzis, S. Triantafyllou, An extended B-spline-based material point method for contact problems, Internat. J. Numer. Methods Engrg. 126 (3) (2025) e70003, http://dx.doi.org/10.1002/nme.70003.
[91] C. Liu, W. Sun, ILS-MPM: An implicit level-set-based material point method for frictional particulate contact mechanics of deformable particles, Comput. Methods Appl. Mech. Engrg. 369 (2020) 113168, http://dx.doi.org/10.1016/j.cma.2020.113168.
[92] D. Kamensky, M.-C. Hsu, D. Schillinger, J.A. Evans, A. Aggarwal, Y. Bazilevs, M.S. Sacks, T.J. Hughes, An immersogeometric variational framework for fluid–structure interaction: Application to bioprosthetic heart valves, Comput. Methods Appl. Mech. Engrg. 284 (2015) 1005–1053, http://dx.doi.org/10.1016/j.cma.2014.10.040, Isogeometric Analysis Special Issue.
[93] S.C. Divi, C.V. Verhoosel, F. Auricchio, A. Reali, E.H. van Brummelen, Error-estimate-based adaptive integration for immersed isogeometric analysis, Comput. Math. Appl. 80 (11) (2020) 2481–2516, http://dx.doi.org/10.1016/j.camwa.2020.03.026, High-Order Finite Element and Isogeometric Methods 2019.
[94] C.V. Verhoosel, E. Harald van Brummelen, S.C. Divi, F. de Prenter, Scan-based immersed isogeometric flow analysis, in: Frontiers in Computational Fluid-Structure Interaction and Flow Simulation: Research from Lead Investigators under Forty - 2023, Springer International Publishing, Cham, 2023, pp. 477–512, http://dx.doi.org/10.1007/978-3-031-36942-1_14.